Ca2+ sensor-mediated ROS scavenging suppresses rice immunity and is exploited by a fungal effector

Mingjun Gao, Yang He, Xin Yin, Xiangbin Zhong, Bingxiao Yan, Yue Wu, Jin Chen, Xiaoyuan Li, Keran Zhai, Yifeng Huang, et al.

Cell

Ca^{2+} sensor-mediated ROS scavenging suppresses rice immunity and is exploited by a fungal effector

Graphical abstract

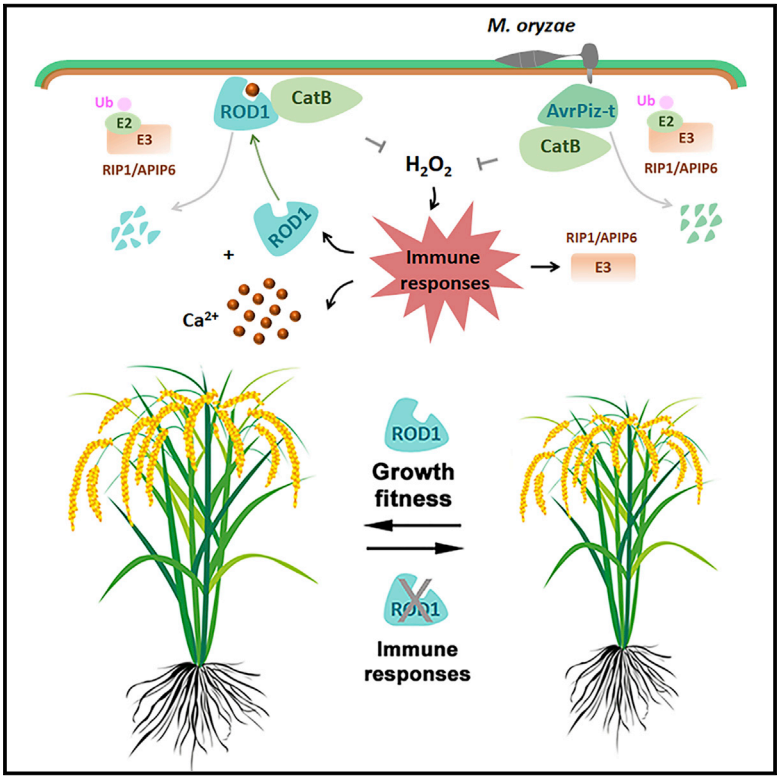

Highlights

- Rice ROD1 suppresses immunity via catalase activation and ROS scavenging
- ROD1 is a Ca^{2+}-sensor fine-tuned by ubiquitination-mediated protein degradation
- Natural *ROD1* variants influence *indica* and *japonica* rice immunity
- The fungal effector AvrPiz-t exploits the ROD1 cascade to promote virulence

Authors

Mingjun Gao, Yang He, Xin Yin, ..., Guo-Liang Wang, Weibing Yang, Zuhua He

Correspondence

xb-zhong@fafu.edu.cn (X.Z.), wbyang@cemps.ac.cn (W.Y.), zhhe@cemps.ac.cn (Z.H.)

In brief

ROD1 encodes a Ca^{2+} sensor to suppress rice immunity by promoting ROS scavenging. The fungal effector AvrPiz-t structurally mimics ROD1 and shares the same ROS-elimination cascade to suppress rice immunity and promote virulence.

Gao et al., 2021, Cell *184*, 5391–5404
October 14, 2021
https://doi.org/10.1016/j.cell.2021.09.009

CellPress

Cell

CellPress
OPEN ACCESS

Article

Ca^{2+} sensor-mediated ROS scavenging suppresses rice immunity and is exploited by a fungal effector

Mingjun Gao,[1,11] Yang He,[1,11] Xin Yin,[1,9,11] Xiangbin Zhong,[1,10,11,*] Bingxiao Yan,[1] Yue Wu,[1] Jin Chen,[1] Xiaoyuan Li,[2] Keran Zhai,[1] Yifeng Huang,[1] Xiangyu Gong,[1] Huizhong Chang,[1] Shenghan Xie,[2] Jiyun Liu,[1] Jiaxing Yue,[3] Jianlong Xu,[4] Guiquan Zhang,[5] Yiwen Deng,[1] Ertao Wang,[1] Didier Tharreau,[6] Guo-Liang Wang,[7] Weibing Yang,[1,8,*] and Zuhua He[1,12,*]

[1]National Key Laboratory of Plant Molecular Genetics, CAS Center for Excellence in Molecular Plant Sciences, Institute of Plant Physiology and Ecology, Chinese Academy of Sciences, Shanghai 200032, China
[2]School of Life Science and Technology, ShanghaiTech University, Shanghai 201210, China
[3]Sun Yat-sen University Cancer Center, Guangzhou 510060, China
[4]Insititute of Crop Sciences, Chinese Academy of Agricultural Sciences, Beijing 100081, China
[5]College of Agriculture, South China Agricultural University, Guangzhou 510642, China
[6]PHIM, CIRAD, INRAE, IRD, Montpellier SupAgro, MUSE, Montpellier Cedex 05, France
[7]Department of Plant Pathology, Ohio State University, OH 43210, USA
[8]CAS-JIC Center of Excellence for Plant and Microbial Sciences, Institute of Plant Physiology and Ecology, Chinese Academy of Sciences, Shanghai 200032, China
[9]State Key Laboratory of Plant Genomics, Institute of Microbiology, Chinese Academy of Sciences, Beijing 100101, China
[10]Present address: College of Resources and Environment and Haixia Institute of Science and Technology, Fujian Agriculture and Forestry University, Fuzhou 350002, China
[11]These authors contributed equally
[12]Lead contact
*Correspondence: xb-zhong@fafu.edu.cn (X.Z.), wbyang@cemps.ac.cn (W.Y.), zhhe@cemps.ac.cn (Z.H.)
https://doi.org/10.1016/j.cell.2021.09.009

SUMMARY

Plant immunity is activated upon pathogen perception and often affects growth and yield when it is constitutively active. How plants fine-tune immune homeostasis in their natural habitats remains elusive. Here, we discover a conserved immune suppression network in cereals that orchestrates immune homeostasis, centering on a Ca^{2+}-sensor, RESISTANCE OF RICE TO DISEASES1 (ROD1). ROD1 promotes reactive oxygen species (ROS) scavenging by stimulating catalase activity, and its protein stability is regulated by ubiquitination. ROD1 disruption confers resistance to multiple pathogens, whereas a natural *ROD1* allele prevalent in *indica* rice with agroecology-specific distribution enhances resistance without yield penalty. The fungal effector AvrPiz-t structurally mimics ROD1 and activates the same ROS-scavenging cascade to suppress host immunity and promote virulence. We thus reveal a molecular framework adopted by both host and pathogen that integrates Ca^{2+} sensing and ROS homeostasis to suppress plant immunity, suggesting a principle for breeding disease-resistant, high-yield crops.

INTRODUCTION

In the absence of specialized immune cells, plants have developed an elaborate immune machinery, composed of microbe- or pathogen-associated molecular patterns (MAMPs/PAMPs)-triggered immunity (PTI) and effector-triggered immunity (ETI), to defend against pathogens (Jones and Dangl, 2006; Macho and Zipfel, 2014). Activation of plant immunity leads to apoplastic reactive oxygen species (ROS) production, cytosolic Ca^{2+} elevation, kinase cascade activation, and localized cell death known as the hypersensitive response (HR) (Boller and Felix, 2009; Spoel and Dong, 2012; Zipfel and Oldroyd, 2017). Immune activation confers resistance against invading pathogens, but constitutive immune responses are costly and impede growth and environmental fitness (Bomblies et al., 2007; Deng et al., 2020; Huot et al., 2014; Tian et al., 2003; Todesco et al., 2010). Plant immunity therefore requires precise control to allow rapid responses upon pathogen infection while minimizing growth penalties under normal conditions. This is particularly important for field crops, which are constantly challenged by diverse pathogens (Brown, 2002; Ning et al., 2017). An energy-efficient and flexible immune system is advantageous for plant survival and crop production (Barabaschi et al., 2020; Nobori and Tsuda, 2019). Understanding how plants fine-tune immune homeostasis in diverse environments is critical for promoting secure crop production.

Various mechanisms have been deployed by plants to reduce the potential cost of excessive immune responses. For instance, expression of plant defense genes exhibits a rhythmic pattern under normal conditions, which enables anticipation of potential

pathogen threat (Goodspeed et al., 2012; Wang et al., 2011; Zhou et al., 2015). Plants can also be primed to a sensitized state after initial infection. This low level of basal immunity allows rapid activation upon subsequent pathogen attack (Conrath et al., 2015). In addition, plants have evolved a number of factors that act to attenuate immune responses, such as the immune suppressors EDR1 (Frye et al., 2001) and MLO (Kim et al., 2002), or guarded positive immune regulators including LSD1 and AtSR1/CAMTA3 (Bonardi et al., 2011; Dietrich et al., 1997; Du et al., 2009; Lolle et al., 2017).

To facilitate infection, pathogens, in turn, have evolved mechanisms that hijack host cellular processes or immune modules through ETS pathways (van Schie and Takken, 2014; Upson et al., 2018). Recently, it was reported that the bacterial effector HopBF1 mimics a host HSP90 client to facilitate pathogenicity (Lopez et al., 2019), and virus proteins have co-opted two subcellular targeting systems to impair salicylic acid (SA)-mediated defense (Medina-Puche et al., 2020). Like SA, ROS plays a central role in plant defense (Boller and Felix, 2009; Chen et al., 1993; Qi et al., 2017; Zhang et al., 2004). ROS homeostasis must be tightly controlled to prevent plant cell damage (Waszczak et al., 2018; Yuan et al., 2017a), potentially presenting a point of interference for pathogen effectors (Guo et al., 2019; Hemetsberger et al., 2012). However, whether plants and pathogens have adopted the same ROS-scavenging mechanism to fine-tune or suppress host immunity is unknown.

Here, we have conducted a long-term study to track the rice susceptibility-like gene *RESISTANCE OF RICE TO DISEASES1* (*ROD1*). *ROD1* encodes a C2 domain Ca^{2+} sensor that acts as a global regulator of immunity. We show that ROD1 promotes H_2O_2 degradation by activating a catalase, CatB. ROD1 stability is fine-tuned by a pair of E3 ubiquitin ligases RIP1 and APIP6. *ROD1* loss-of-function leads to robust and broad-spectrum resistance to multiple bacterial and fungal pathogens. ROD1 has a six-strand antiparallel β sheet structure, which is also found in a fungal blast effector, AvrPiz-t (de Guillen et al., 2015). ROD1 and AvrPiz-t share the same protein degradation and ROS-elimination cascade, supporting a model where a fungal effector has exploited the host protein-mediated immune regulation. We identify a naturally occurring, locally adaptive *ROD1* allele that confers higher basal resistance without loss of crop yield, underlining the importance of this factor in balancing immunity and growth. Our study thus reveals a previously unrecognized mechanism where plant and pathogen factors suppress plant immune responses through the same cascade.

RESULTS

rod1 rice shows broad-spectrum disease resistance to multiple pathogens

Rice productivity is threatened by three major diseases: rice blast caused by the hemibiotrophic fungus *Magnaporthe oryzae* (*M. oryzae*), bacterial blight caused by *Xanthomonas oryzae* pv. *oryzae* (*Xoo*), and sheath blight caused by the necrotrophic fungus *Rhizoctonia solani* (*R. solani*). Through a large-scale screen of rice germplasms and breeder's collections, we identified a natural recessive broad-spectrum disease resistance variant, *resistance of rice to diseases1 (rod1)*, from a TP309 (*japonica* rice) breeding population. The *rod1* variant exhibits strong resistance to rice blast, sheath blight, and bacterial blight (Figures 1A–1C).

Compared to TP309, *rod1* accumulated much higher levels of SA and jasmonic acid (JA) (Figure 1D), indicating constitutive defense activation. In support of this, RNA sequencing (RNA-seq) analysis revealed that genes involved in ROS homeostasis and cell wall reinforcement were highly enriched, whereas genes related to Ca^{2+}-binding were downregulated in *rod1* (Figures 1E and 1F; Table S1). These data suggest a link between ROS metabolism and Ca^{2+}-signaling in *ROD1*-mediated immune regulation. Constitutively activated immunity in *rod1* mutants compromised plant growth, leading to reduced grain yield. However, in a natural blast nursey trial, *rod1* showed better growth and produced more seeds than TP309 (Figures 1G and 1H). This indicates superiority of the *rod1* allele under disease stress.

ROD1 is a specific type of host susceptibility gene conserved in cereals

We identified the *ROD1* gene by map-based cloning. Using a large mapping population derived from a cross between *rod1* and an *indica* accession Taichung Native1 (TN1), *ROD1* was mapped to a 53-kb region near the telomere of chromosome 6 (Figure S1A). Comparison of TP309, Nipponbare (*japonica*, the reference genome), and *rod1* DNA sequences revealed a single nucleotide deletion in the exon of *LOC_Os06 g03810*, that causes a frameshift in *rod1* (Figure S1B). The identity of the *ROD1* gene was confirmed using genetic complementation with a fragment containing the *LOC_Os06 g03810* genomic sequence and 3,000-bp promoter region (Figure S1C). ROD1 protein is predicted to be 225 amino acids (aa) long and contains a C2 domain (Figure 2A). To further assess the role of *ROD1* in disease resistance, we overexpressed *ROD1* in TP309 using the maize *Ubiquitin* (*Ubi*) promoter (Figures S1D and S1E). The *Ubi::ROD1* transgenic plants displayed increased susceptibility (Figures S1F–S1H), demonstrating that ROD1 is likely a suppressor of rice immunity.

In situ hybridization revealed that *ROD1* is predominantly expressed in leaves, a common site of pathogen infection (Figure 2B). The expression of *ROD1* could be induced by pathogen infection (Figure 2C). *ROD1* is also highly expressed in the inflorescence meristem (IM) and young panicles (Figure S1I), implying a potential role in reproductive growth. Indeed, IM development was largely delayed in *rod1* plants, leading to reduced seed production (Figures S1J–S1L). Conversely, overexpression of *ROD1* using its endogenous promoter (*pROD1::ROD1*) promoted panicle growth and increased grain yield (Figures S1K and S1L). Therefore, ROD1 plays distinct roles in rice disease resistance and growth fitness.

ROD1 orthologs are found across the flowering plants (angiosperms) but not in lower plant lineages (e.g., chlorophytes, mosses, and Marchantia) or early vascular plants such as fern (Figures S2A and S2B), suggesting that this class of C2 domain proteins emerged during a relatively late stage in plant evolution. ROD1-like proteins have high sequence similarity in monocot crops, but have diverged in *Brassicaceae* such as *Arabidopsis thaliana* (Figure S2B). We therefore tested whether ROD1-like proteins play a conserved role in immunity in cereals. Maize

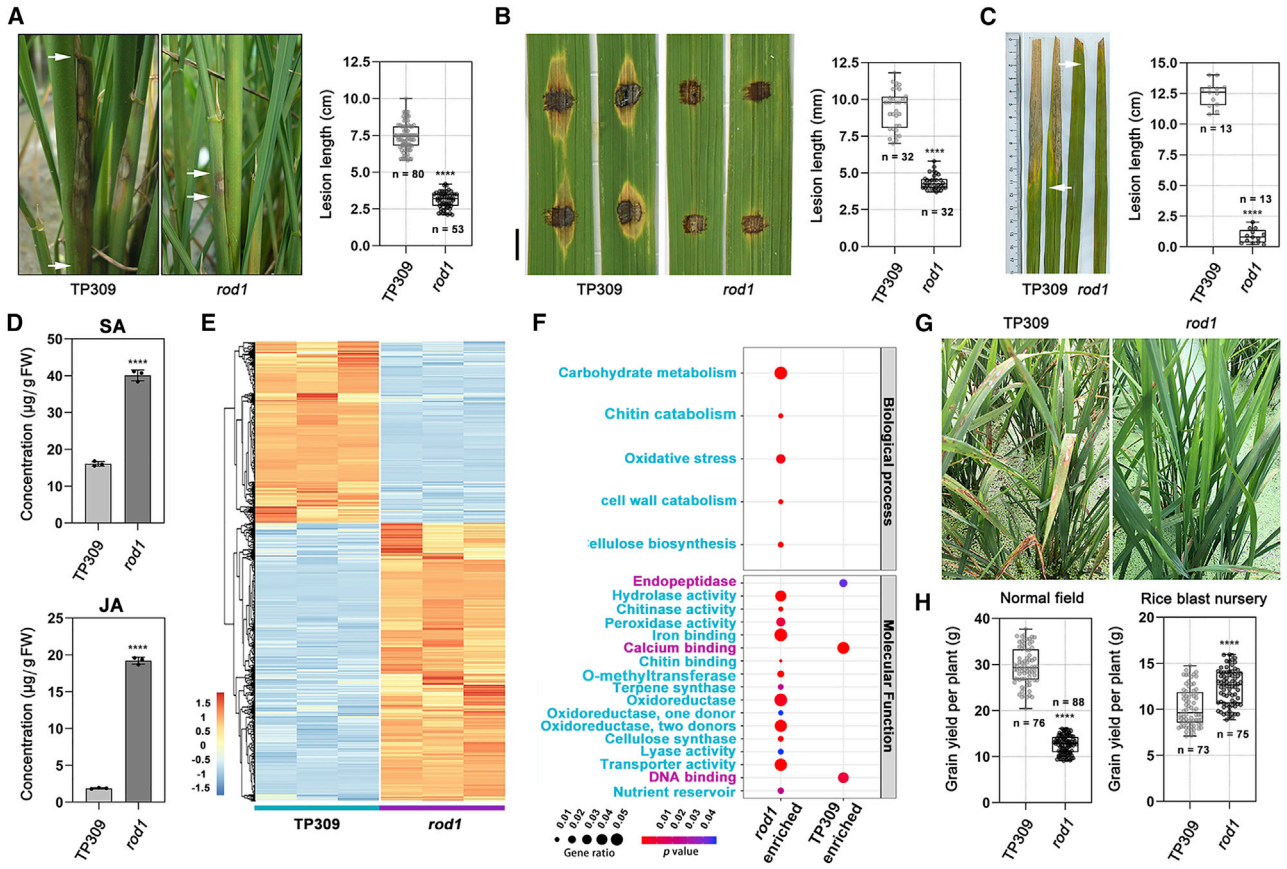

Figure 1. *rod1* plants show multiple disease resistance

(A) Increased sheath blight resistance of *rod1*. The wild-type parent (TP309) and *rod1* plants were inoculated with *R. solani* at tillering stage in the rice paddy. The lesion length was measured at 7 days post-inoculation (dpi).

(B) Increased blast resistance of *rod1*. Leaves were punch-inoculated with *M. oryzae*. The lesion length was measured at 7 dpi. Scale bar, 5 mm.

(C) Increased bacterial blight resistance is seen in the *rod1* mutant. Leaves were inoculated with *Xoo* strain PXO99A. The lesion length was measured at 14 dpi.

(D) Measurement of SA and JA levels in TP309 and *rod1* leaves. Error bars, mean ± SD (n = 3).

(E and F) Hierarchical clustering (E) and Gene Ontology (GO) (F) analysis of differentially expressed genes in TP309 and *rod1* leaves. Note that genes involved in calcium binding, DNA binding and endopeptidases were downregulated in *rod1* compared with TP309 (see also Table S1).

(G) Field blast resistance of TP309 and *rod1* grown in the natural nursery.

(H) Grain yield of TP309 and *rod1* under natural non-diseased (normal field) and diseased (blast nursery) conditions. ****$p < 0.0001$ (two-tailed t test, compared to TP309).

Data in (A)–(C) and (H) are displayed as box and whisker plots with individual data points. The error bars represent maximum and minimum values. Center line, median; box limits, 25th and 75th percentiles.

See also Figures S1 and S2.

mutant of *GRMZM2G069335* (here referred to as *ZmROD1*) was generated using CRISPR/Cas technology (Figure S2C). Compared to wild-type (WT), the *ZmROD1* mutant (*CR-zmrod1*) showed enhanced *PR* gene expression (Figure S2D) and increased resistance to *R. solani* (Figure S2E), suggesting that *ROD1* and its orthologs constitute a specific type of susceptibility genes that play a conserved role across cereal plants.

ROD1 encodes a Ca^{2+} sensor protein

C2 domains typically act as Ca^{2+} sensors that bind to phosphoinositide lipids in a Ca^{2+}-dependent manner, thereby targeting proteins to specific membrane regions (Clapham, 2007; Rizo and Südhof, 1998). Using the microscale thermophoresis (MST) assay with purified recombinant ROD1 proteins produced in *E. coli*, we confirmed that ROD1 binds to Ca^{2+} with high affinity (Figure 2D). The aspartic acid residues (D) of C2 domains are responsible for Ca^{2+} binding. We identified four D sites in ROD1 (D72, D85, D132, and D135). When these sites were substituted with asparagine (N), the Ca^{2+} binding activity of the mutated proteins, $ROD1^{D132N}$ and $ROD1^{D\text{-}quad}$, was greatly reduced (Figure 2D). Ca^{2+} changes the electrostatic properties of C2 domains, enabling them to bind to negatively charged phosphoinositide lipids (Murray and Honig, 2002). To assess the lipid binding capacity and specificity of ROD1, we incubated GST-ROD1 fusion protein with various lipids. ROD1 strongly associated with PI(4)P, PI(5)P, PI(3,5)P2, and had weaker affinity

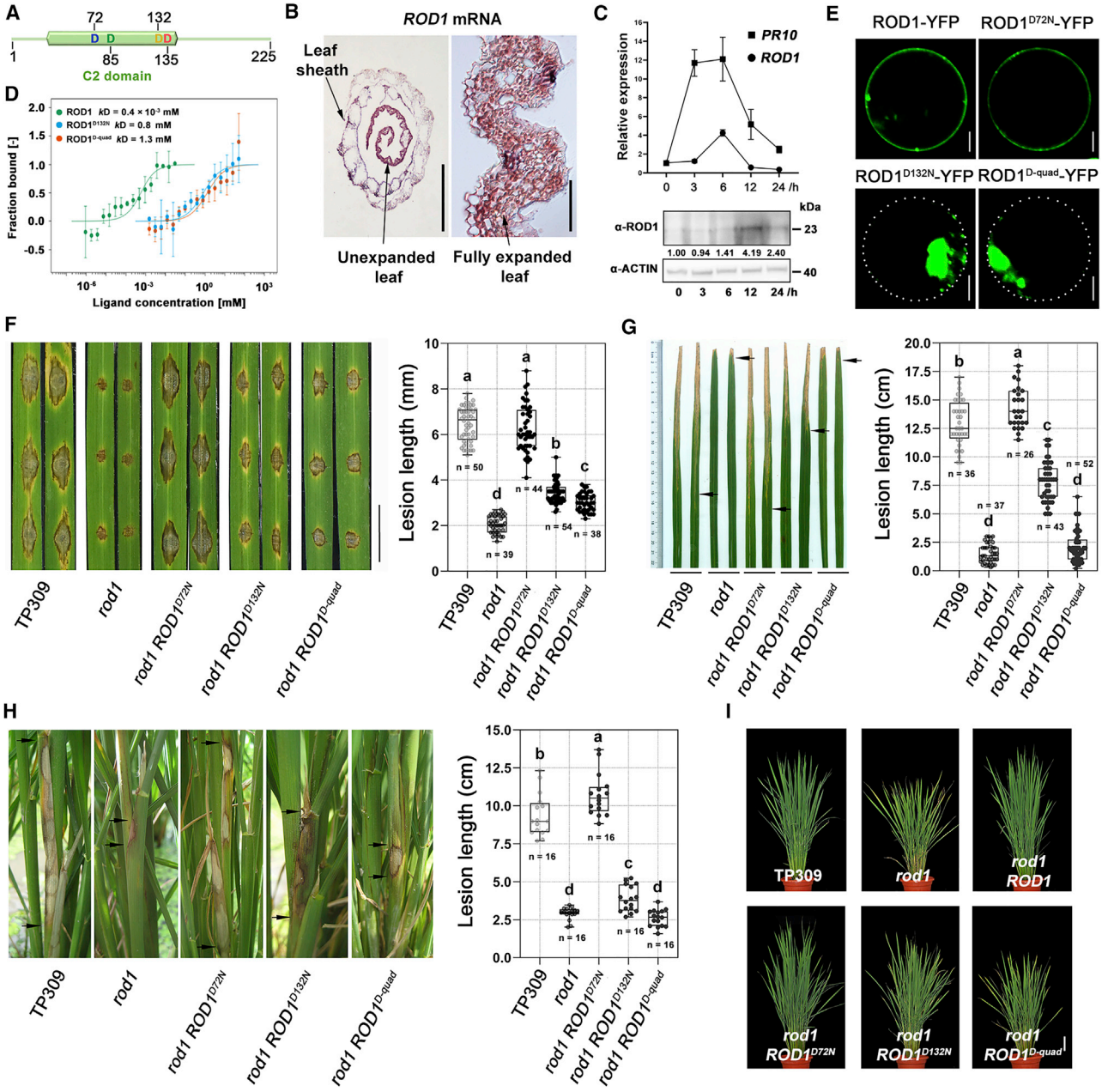

Figure 2. ROD1 binds to Ca^{2+} to modulate immunity

(A) Schematic diagram of ROD1. ROD1 contains a C2 domain with four aspartic acid (D) residues.

(B) Detection of *ROD1* mRNAs in leaves by RNA *in situ* hybridization. Scale bar, 100 μm.

(C) Induction of *ROD1* during pathogen infection. Field-grown plants were inoculated with *Xoo* at the booting stage, and leaf samples were collected over a 0–24 hpi time course. *PR10* induction was followed to indicate immune activation. *ROD1* transcript levels (top panel) were detected by qRT-PCR, and ROD1 proteins (bottom panel) were detected by immunoblotting using an anti-ROD1 antibody. Rice actin served as a loading control. Error bars, mean ± SD (n = 3).

(D) MST assay showing Ca^{2+} binding of ROD1. $ROD1^{D132N}$; $ROD1^{D\text{-}quad}$ (carrying mutations at 4 residues, D72, D85, D132, and D135). Both ROD1 mutants largely lost Ca^{2+} binding capacity. The solid curve is the fit of the data points to the standard KD-Fit function. Each binding assay was repeated three times independently, and bars represent standard deviations. K_d, dissociation constant.

(E) Ca^{2+} binding is required for ROD1 plasma membrane localization. ROD1 and the mutated variants were fused with YFP and expressed in rice protoplasts. Dashed lines in the bottom two panels label cell boundaries. Scale bars, 5 μm.

(F–H) Ca^{2+} binding mutation abolished ROD1-mediated immune suppression. The ROD1 mutant variants ($ROD1^{D72N}$, $ROD1^{D132N}$, and $ROD1^{D\text{-}quad}$) were expressed in *rod1* plants under the *ROD1* promoter. Plants were inoculated with *M. oryzae* (F), *R. solani* (G), and *Xoo* (H). Data are displayed as box and whisker plots

(legend continued on next page)

to PI(4,5)P2 and PA (Figure S3A). Lipid binding by ROD1 was abolished in the presence of EGTA, a specific Ca^{2+} chelator. $ROD1^{D\text{-}quad}$ also failed to bind to lipids (Figure S3A), indicating that Ca^{2+} binding is a prerequisite for ROD1-lipid interaction.

Protein localization analysis showed that ROD1 is predominantly distributed at the cell periphery associated with the plasma membrane (PM), forming dispersed punctate structures (Figure S3B). Mutation of aspartic acid residues in the ROD1 C2 domain severely disrupted subcellular localization: the resulting YFP-$ROD1^{D132N}$, YFP-$ROD1^{D\text{-}doub}$, YFP-$ROD1^{D\text{-}trip}$, and YFP-$ROD1^{D\text{-}quad}$ proteins aggregated into large cytoplasmic patches (Figures 2F, S3C, and S3D). Interestingly, treatment with the PAMP elicitor (flg22) enhanced the PM accumulation of ROD1 (Figures S3E and S3F), implying that immune activation promotes localization of ROD1 to the PM.

We next used a genetic approach to investigate the role of Ca^{2+}-sensing in ROD1-mediated immune suppression. ROD1 Ca^{2+}-binding variants were expressed in *rod1* under the control of the endogenous *ROD1* promoter. $ROD1^{D132N}$ and $ROD1^{D\text{-}quad}$, which are defective in Ca^{2+}-binding and PM localization, failed to rescue the growth phenotypes of *rod1*, and the transgenic plants still exhibited high resistance to different rice pathogens (Figures 2F–2I). These results collectively indicate that Ca^{2+}-binding enables ROD1 association with phospholipids and PM localization. These molecular and cellular events are crucial for ROD1 function in immunity and plant growth regulation.

Two E3 ubiquitin ligases fine-tune ROD1 protein stability

The functions of single C2 domain proteins have not been well documented in plants. To elucidate the molecular mechanisms underlying ROD1-mediated suppression of immunity, we conducted a yeast two-hybrid (Y2H) screen to identify ROD1 interacting proteins. Using ROD1 as a bait, we screened a cDNA library generated from *M. oryzae*-infected rice leaves (Zhai et al., 2019) and uncovered two RING E3 ubiquitin ligases, ROD1 interacting protein 1 (RIP1) and AvrPiz-t interacting protein 6 (APIP6) (Park et al., 2012) (Figures S4A–S4D). Both *RIP1* and *APIP6* mRNAs are expressed in leaves (Figure S4E), and are induced by pathogen infection (Figure S4F). Similar to APIP6 (Park et al., 2012), RIP1 also possesses E3 ubiquitin ligase activity (Figure S4G). When the TF-ROD1 fusion protein was incubated with either RIP1 or APIP6, high molecular weight bands were detected (Figures 3A and S4H). These bands were lost in the RIP1 H74Y or APIP6 H58Y mutants that lack ubiquitin ligase activity, suggesting that ROD1 is ubiquitinated by RIP1 and APIP6.

To determine the effect of ubiquitin modification on ROD1 protein stability, we generated *RIP1* and *APIP6* knockout mutants using CRISPR/Cas9 (*CR-rip1* and *CR-apip6*) (Figure 3B). We also generated plants overexpressing these factors using the maize *Ubi1* promoter. ROD1 protein levels in the *Ubi::RIP1* and *Ubi::APIP6* plants, as detected by immunoblotting with an anti-ROD1 antibody, were reduced. Conversely, ROD1 was stabilized in the *CR-rip1* and *CR-apip6* mutants (Figure 3C). Together, these *in vitro* and *in planta* assays indicate that RIP1 and APIP6 target ROD1 for ubiquitin-mediated degradation.

To investigate the immune output of RIP1- and APIP6-mediated ROD1 destruction, we analyzed disease resistance of the *RIP1* and *APIP6* transgenic plants. Both *CR-rip1* and *CR-apip6* plants showed compromised resistance to *M. oryzae*, *R. solani*, or *Xoo*. In contrast, *RIP1* and *APIP6* overexpression resulted in enhanced resistance to these pathogens (Figures 3D and 3E), indicating that RIP1 and APIP6-mediated turnover of ROD1 levels regulates immune activation.

ROD1 stimulates catalase activity to eliminate ROS

Our Y2H screen also recovered a catalase, CatB, as a candidate ROD1 binding factor (Figures S5A and S5B). The interaction between ROD1 and CatB was validated by split luciferase complementation (SLC) and co-immunoprecipitation (coIP) assays (Figures 4A and 4B). Catalase is a ROS scavenging enzyme that catalyzes H_2O_2 turnover, which has been shown to inhibit immunity in *Arabidopsis* (Yuan et al., 2017a). We found that the rice *CR-catb* mutant generated by CRISPR/Cas9 showed higher *PR* gene expression and enhanced disease resistance, indicating a negative role for *CatB* in rice immune responses (Figures S5A–S5D).

To determine the biological significance of the ROD1-CatB interaction, we first investigated the effect of ROD1 on the biochemical activity of CatB. We found that CatB-mediated H_2O_2 degradation was accelerated by ROD1 but not the Ca^{2+}-binding mutants $ROD1^{D132N}$ or $ROD1^{D\text{-}quad}$ (Figures 4C and 4D), suggesting that ROD1 stimulates CatB activity in a Ca^{2+}-dependent manner. We ectopically expressed CatB-FLAG in TP309 and *rod1* plants, and purified the fusion proteins through immunoprecipitation with an anti-FLAG antibody. We found that the H_2O_2 degradation activity of CatB-FLAG isolated from the *rod1* background was lower than CatB-FLAG from TP309 (Figure 4E), indicating that ROD1 indeed contributes to CatB activity *in planta*. Further supporting this conclusion, H_2O_2 scavenging activity in total protein extracts from *rod1* leaves was 65% of that from TP309 control. *ROD1* overexpression increased catalase activity by ~30% (Figure 4F). Consequently, *rod1* plants accumulated higher levels of H_2O_2 than WT (Figures 4G and 4H). Moreover, elicitor (flg22)-induced H_2O_2 production was enhanced in *rod1*, but compromised in *ROD1* overexpression plants (Figure 4I), suggesting a role for ROD1 in immune suppression through promoting ROS scavenging.

GFP-CatB protein was mainly localized in the peroxisomes, whereas we also detected weak fluorescence signals at the PM (Figure 4J), consistent with previous findings (Zhang et al., 2016). Peroxisomal CatB protein levels were reduced when

with individual data points. The error bars represent maximum and minimum values. Center line, median; box limits, 25th and 75th percentiles. Significant differences were determined by Duncan's new multiple range test and indicated with different letters. Scale bar in (F), 5 mm.

(I) Morphology of TP309, *rod1*, and *rod1* expressing various mutated ROD1 proteins defective in Ca^{2+} binding, showing that $ROD1^{D72N}$ largely restored the *rod1* growth, similar to ROD1. Scale bar, 5 cm.

See also Figure S3.

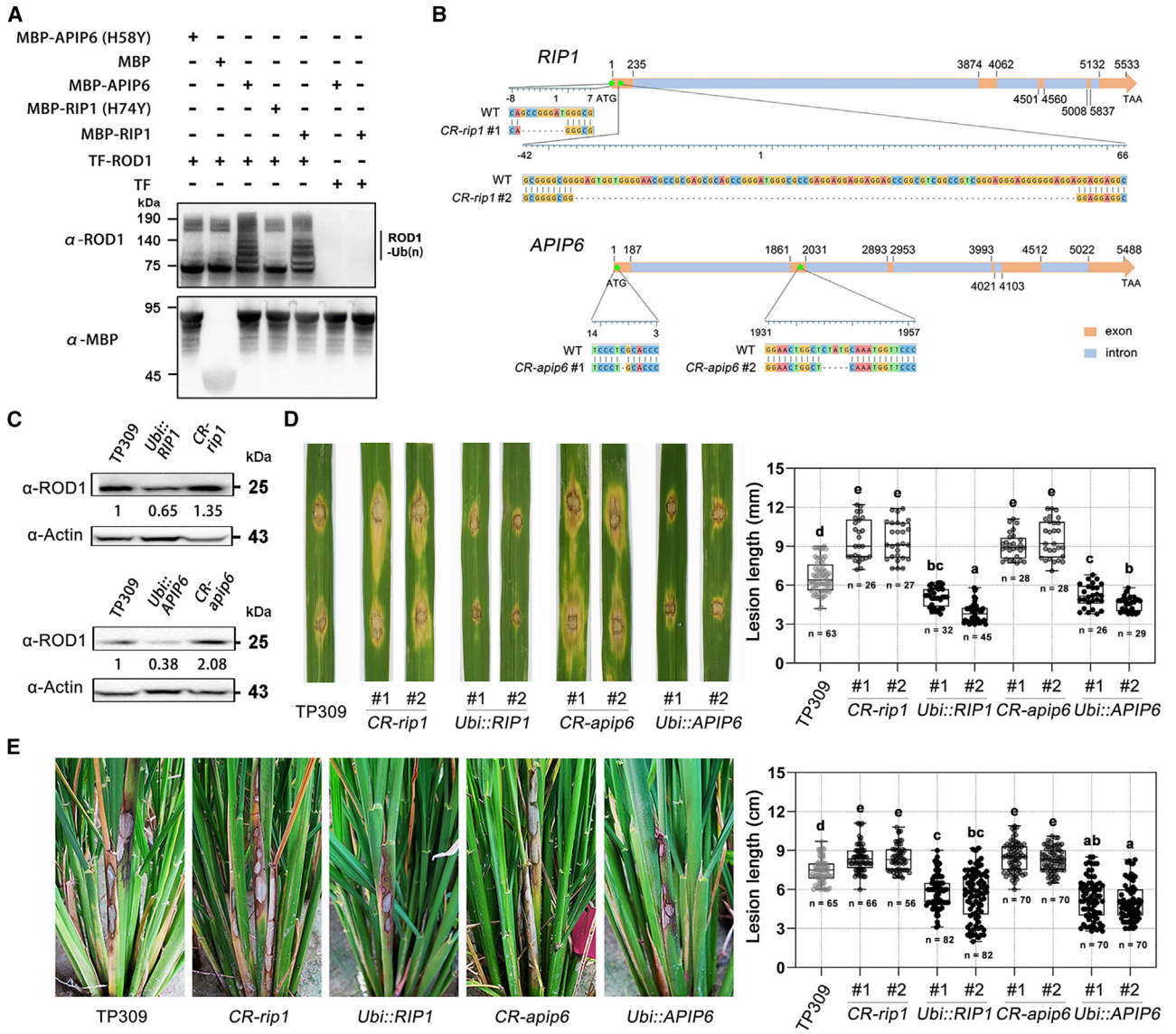

Figure 3. ROD1 protein stability is controlled by a pair of E3 ubiquitin ligases

(A) Ubiquitination of ROD1 by the E3 ligases RIP1 and APIP6. Mutated MBP-RIP1 (H74Y) and MBP-APIP6 (H58Y) were used as negative controls. The experiment was independently repeated twice with similar results.

(B) Generation of *RIP1* and *APIP6* knockout lines by CRISPR/Cas9. Two target sites in exon one of *RIP1*, and two separate sites located in exon 1 and exon 2 of *APIP6* were targeted to create loss of function mutants (*CR*) of either *RIP1* or *APIP6*.

(C) ROD1 protein levels in *RIP1* and *APIP6* overexpression and *CR* mutant plants. An anti-ROD1 antibody was used to detect endogenous ROD1. Note that overexpression of *RIP1* or *APIP6* reduced ROD1 abundance, while their mutations stabilized ROD1.

(D) *RIP1* and *APIP6* positively regulate blast resistance. Two representative *CR* and overexpression lines were compared with wild-type TP309.

(E) *RIP1* and *APIP6* positively regulate sheath blight resistance in the *CR* and overexpression lines compared to wild-type TP309.

Data in (D) and (E) are displayed as box and whisker plots with individual data points. The error bars represent maximum and minimum values. Center line, median; box limits, 25th and 75th percentiles. Significant differences were determined by Duncan's new multiple range test and indicated with different letters.

See also Figure S4.

co-expressed with mCherry-ROD1, and the majority of GFP-CatB signal was instead found at the PM (Figure 4J). This is reminiscent of STRK1- and CPK8-mediated PM re-localization of catalases in rice and *Arabidopsis*, respectively (Zhou et al., 2018; Zou et al., 2015). Our data indicate that ROD1 promotes localization of CatB to the PM. This was further verified in the bimolecular fluorescence complementation (BiFC) assay, showing that the interaction between ROD1 and CatB occurs mainly at the PM region (Figure 4K).

Finally, we evaluated the effect of the ROD1-CatB interaction on plant immune responses. Using the cell death assay in *N. benthamiana*, we found that the MLA10-induced

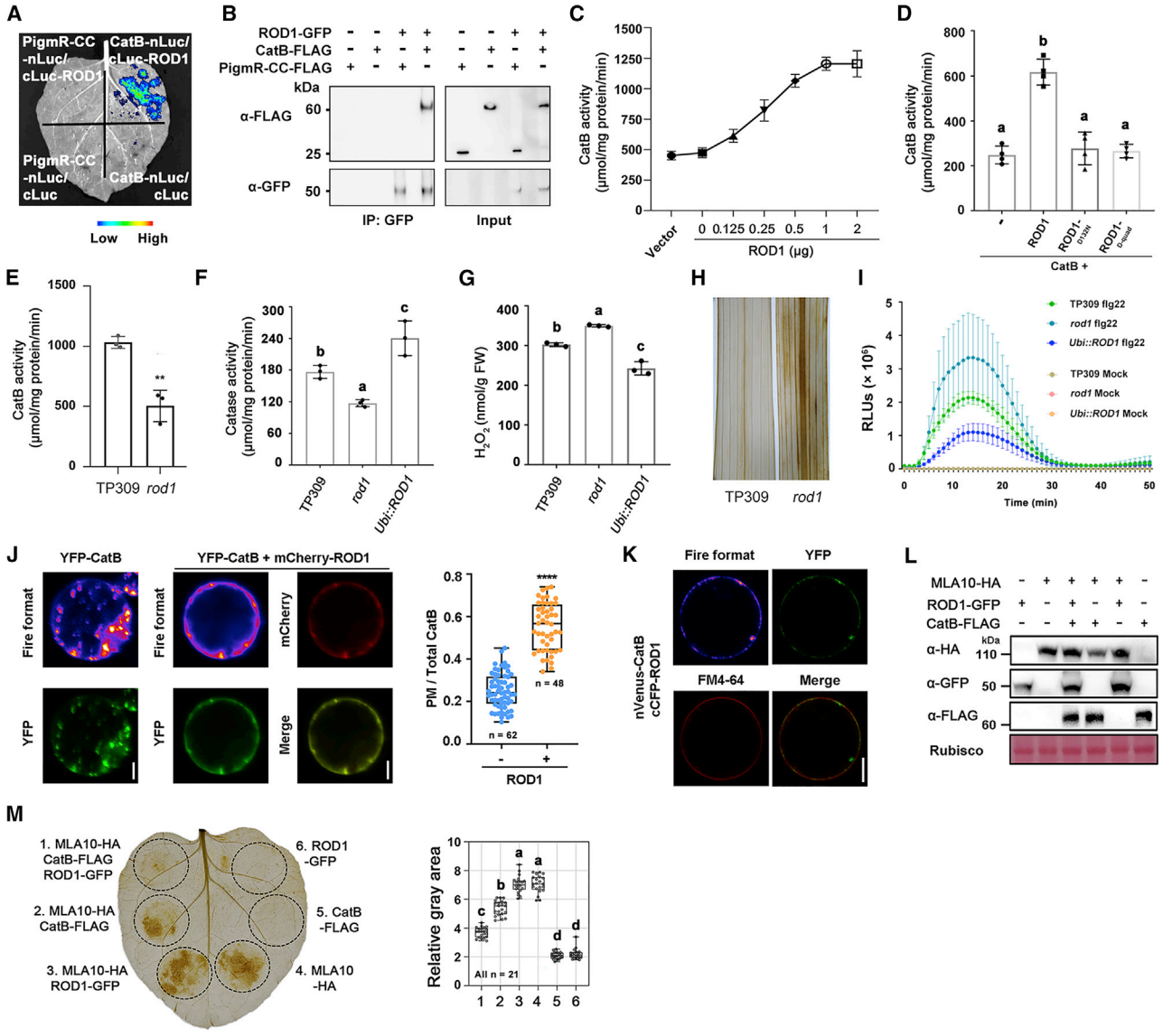

Figure 4. ROD1 stimulates catalase activity to eliminate H_2O_2

(A and B) Interaction of ROD1 with CatB detected by split luciferase complementation (SLC) (A) and coIP (B) assays. The coiled-coil (CC) domain of the NLR protein PigmR (PigmR-CC), which does not interact with CatB, was used as a negative control.

(C) ROD1 enhanced the H_2O_2 degradation activity of CatB. Purified CatB protein was used for *in vitro* catalase assay in the presence of differing amounts of ROD1 (n = 3).

(D) CatB-mediated H_2O_2 degradation in the presence of ROD1 or its Ca^{2+}-binding mutants. Compared to ROD1, CatB activity was lower when co-inoculated with ROD1 Ca^{2+}-binding mutants, suggesting that ROD1 stimulates CatB activity in a Ca^{2+}-dependent manner. Significant differences were determined by Duncan's new multiple range test and indicated with different letters (n = 4).

(E) Analysis of *in vivo* catalase activity using CatB-FLAG fusion proteins extracted from TP309 and *rod1* transgenic plants. CatB-FLAG proteins were purified by immunoprecipitation (IP) using an anti-FLAG antibody. **p < 0.01 (two-tailed t test, compared to TP309) (n = 3).

(F) Analysis of *in vivo* catalase activity using total proteins extracted from TP309, *rod1*, and *ROD1* overexpression plants. Significant differences were determined by Duncan's new multiple range test and indicated with different letters (n = 3).

(G) Measurement of H_2O_2 levels in TP309, *rod1*, and *ROD1* overexpression plants. Significant differences were determined by Duncan's new multiple range test and indicated with different letters (n = 3).

(H) Visible detection of ROS in TP309 and *rod1* by DAB staining.

(I) Comparison of elicitor-triggered ROS production in TP309, *rod1*, and *ROD1* overexpression plants. Twelve-day-old rice seedlings were treated with the bacterial PAMP flg22 (1 μM), and ROS was detected using Luminol assay (n = 9).

(J) ROD1 promotes CatB plasma membrane (PM) localization. YFP-CatB was expressed in the absence (left) or presence (right) of mCherry-ROD1 in rice protoplast cells. ****p < 0.0001 (two-tailed t test). Scale bars, 5 μm.

(K) BiFC assay was used to evaluate ROD1-CatB interaction at the PM region. Scale bar, 5 μm.

(legend continued on next page)

hypersensitive response (HR) (Bai et al., 2012) was partially suppressed by CatB, and almost completely abolished by ROD1 and CatB co-expression (Figures 4L and 4M). These results collectively suggest that ROD1 plays dual roles in CatB enzyme activity and subcellular localization: it recruits CatB to the PM and stimulates CatB-mediated ROS scavenging, which ensure spatiotemporal precision of ROS metabolism thus contribute to immune suppression.

A natural *ROD1* variation contributes to subspecies-specific rice field disease resistance

Given the crucial roles of *ROD1* in immune regulation, we next investigated its variation in rice germplasm. Comparison of *ROD1* sequences in different accessions revealed low nucleotide diversity (π = 4.17e−07) (Figure 5A), suggesting a selective sweep at this locus. Among the 12 subgroups of ~3,000 rice collections (Wang et al., 2018), negative Tajima's *D* values were observed mainly in the *indica* but not the *japonica* subgroups (Figure 5B), implying that *ROD1* underwent differential selection during *indica* rice adaptation. From the 262 Asian cultivated rice accessions, we identified two single nucleotide polymorphisms (SNPs) within the *ROD1* coding region, SNP1$^{A/C}$, a non-synonymous nucleotide polymorphism with an amino acid change from proline to threonine, and SNP2$^{G/C}$, a synonymous nucleotide polymorphism (Figures 5C and S6A; Table S2). Based on these two SNPs, the rice cultivars can be grouped into three haplotypes: AG (type I), CG (type II), and AC (type III) (Figure S6A). We randomly selected 178 accessions from these three haplotypes and assayed their basal resistance to *R. solani* in the paddy field. This analysis exploits the fact that no major resistance genes are present against this necrotrophic pathogen in rice (Deng et al., 2020), which would otherwise interfere with the evaluation. We found that the lesion length of type I and type III (both SNP1^{A}) plants was significantly shorter than that of type II (SNP1^{C}) plants (Figure 5D), indicating that SNP1$^{A/C}$ is associated with altered field disease resistance. We next introduced *ROD1* containing either SNP1^{A} or SNP1^{C} into *rod1* and found that both genes could rescue the growth phenotypes of *rod1* (Figure 5E). Although *ROD1*(SNP1^{C}) could fully suppress disease resistance in *rod1* mutants, the effect of *ROD1*(SNP1^{A}) was less robust (Figure 5F), confirming that SNP1$^{A/C}$ indeed impacts basal defense.

To further determine the differential functions of SNP1^{A} and SNP1^{C}, we generated chromosome segment substitution lines (CSSLs) in a high-yield elite rice variety Huajingxian74 (HJX74). The chromosomal region around *ROD1* in HJX74, which contains SNP1^{A}, was substituted with DNA fragments from Katy and Basmati (both harboring SNP1^{C}), giving rise to CSSL-1 and CSSL-2, respectively (Figure S6B). A pathogen inoculation assay showed that, compared to Huajingxian74, the two CSSLs developed larger lesions (Figure 5G), confirming that *ROD1*(SNP1^{A}) is a more resistant allele than *ROD1*(SNP1^{C}). However, no change in grain production was observed for the CSSL lines (Figures S6C and S6D), despite their higher resistance. Our results suggest that the SNP1$^{A/C}$ does not affect growth fitness.

Because *ROD1* mRNA and protein levels were comparable between HJX74, CSSL-1, and CSSL-2 (Figures S6E and S6F), we speculate that this A/C variant might interfere with the activation of CatB by ROD1. To address this possibility, we examined the impact of ROD1 (SNP1^{A}/SNP1^{C}) on CatB-mediated ROS scavenging. We found that CatB was less active in the presence of ROD1 (SNP1^{A}) than ROD1 (SNP1^{C}) (Figure S6G). Consistently, the proteins extracted from *ROD1*(SNP1^{A})/*rod1* complemented plants showed a 10% reduction in H_2O_2 hydrolysis activity compared to those from the *ROD1*(SNP1^{C})/*rod1* plants (Figure S6H). Differential activities of ROD1(SNP1^{A}) and ROD1(SNP1^{C}) were further verified by the tobacco cell death assay, showing that ROD1(SNP1^{A}) only partially enhanced CatB-mediated suppression of MLA10-triggered cell death (Figure S6I). These data together suggest that natural variation of ROD1 modifies its effect on catalase activation and thereby immune regulation.

Analysis of *ROD1* allele frequency in different rice varieties revealed subspecies-specific distribution (Figure S6J). Of the 803 *japonica* varieties analyzed, only 5.6% (45/803) carry the SNP1^{A} allele; in contrast, this allele is present in 57.2% of 1,531 (876/1531) *indica* varieties (Figure 5C). To track the evolutionary origin of SNP1, we compared *ROD1* sequences in 44 wild rice accessions and identified only 4 accessions with SNP1^{A}, whereas the other 40 accessions all contain SNP1^{C}. Therefore, SNP1^{A} is mainly retained in *indica*, whereas SNP1^{C} is predominant in both wild rice and *japonica*. The striking difference in SNP1^{A} and SNP1^{C} distribution between the two rice subspecies prompted us to investigate their geographic distribution. We found that the accessions containing SNP1^{A} are mainly enriched in tropical and subtropical (low-latitude) regions, whereas accessions containing SNP1^{C} tend to be enriched in temperate zones (Figure 5H). Together, these results demonstrate that allelic variation of *ROD1* fine-tunes ROS homeostasis thus contributing to subspecies-specific disease resistance.

The pathogen effector AvrPiz-t structurally mimics ROD1 and activates the ROD1 immune suppression module

Thus far, our data indicate that ROD1, together with the E3 ubiquitinin ligases RIP1, APIP6, and the catalase CatB, comprise a molecular circuitry that regulates rice ROS homeostasis and immunity (Figure 6A). APIP6 was previously reported to interact with and mediate the degradation of AvrPiz-t, an effector secreted by the fungal pathogen *M. oryzae* (Park et al., 2012).

(L and M) ROD1 and CatB compromised the MLA10-triggered hypersensitive response cell death in *N. benthamiana* leaves. The severity of cell death was quantified as relative gray area. The expression of ROD1-eGFP, CatB-FLAG, and MLA10-HA proteins was detected by immunoblot, and Ponceau staining of Rubisco serves as a loading control (L) Significant differences in (M) were determined by Duncan's new multiple range test and indicated with different letters. Error bars in (C)–(G) and (I) represent mean ± SD and in (J) and (M) they represent maximum and minimum values. Center line, median; box limits, 25th and 75th percentiles.

Experiments were repeated three times in (C), (E) and (F) and two times in (A), (B), (D), and (G)–(K) with similar results.

See also Figure S5.

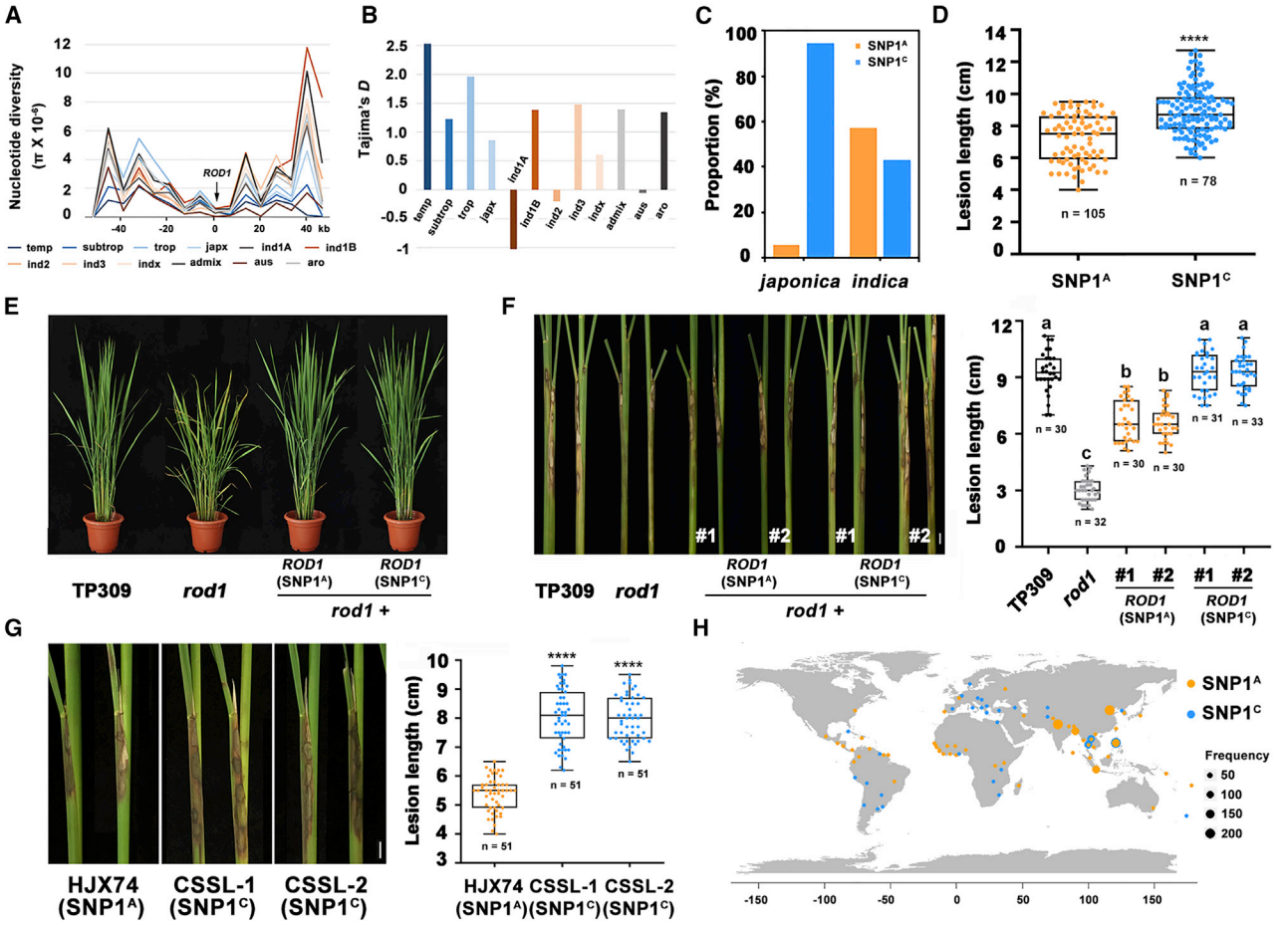

Figure 5. Natural variation of the *ROD1* allele associates with field disease resistance

(A) Nucleotide diversity of *ROD1* and its surrounding 100-kb region in different rice subgroups.

(B) Tajima's *D* values of *ROD1* genomic sequences in the subgroups of cultivated rice.

(C) Proportion of the SNP1^{A} and SNP1^{C} alleles in the two subspecies of cultivated rice. Note that nearly all *japonica* accessions carry SNP1^{C}.

(D) Sheath blight resistance of rice varieties harboring SNP1^{A} and SNP1^{C} in the field. ****$p < 0.0001$ (two-tailed t test).

(E and F) Morphology (E) and disease resistance (F) phenotypes in TP309, *rod1* and *rod1* plants complemented with *ROD1* containing SNP1^{A} or SNP1^{C}. Note that *ROD1*(SNP1^{A}) only partially suppressed the *rod1* resistance phenotype in two representative lines, in comparison to *ROD1*(SNP1^{C}). Significant differences in (F) were determined by Duncan's new multiple range test and indicated with different letters.

(G) Sheath blight resistance of HJX74 (SNP1^{A}) and the CSSL lines (SNP1^{C}) in the field. ****$p < 0.0001$ by two-tailed t test and Bonferroni correction for multiple (two comparisons) tests.

(H) Geographical distribution of the SNP1^{A} and SNP1^{C} alleles in 2624 rice cultivars whose locations/origins are marked with the respective capitals (Wang et al., 2018). Note that the SNP1^{A} allele was enriched in the varieties grown in the tropical and subtropical regions. See also Figure S6.

Data in (D), (F), and (G) are displayed as box and whisker plots with individual data points. The error bars represent maximum and minimum values. Center line, median; box limits, 25th and 75th percentiles.

See also Table S2.

Given the high similarity between RIP1 and APIP6, we tested whether RIP1 also targets AvrPiz-t, and observed that RIP1 interacted with AvrPiz-t (Figure S7A). Hence, both the host susceptibility protein ROD1 and the pathogen virulence protein AvrPiz-t are recognized and destabilized by a common pair of E3 ligases.

AvrPiz-t interferes with host immunity in rice (Park et al., 2012), but the underlying mechanism remains unclear. Because AvrPiz-t and ROD1 are targeted by the same E3 ligases and both suppress plant immunity, we next asked whether AvrPiz-t regulates the same immune regulatory circuitry as ROD1. To address this possibility, we performed Y2H and coIP assays, and found that AvrPiz-t strongly interacts with CatB (Figures S7B and S7C). Next, we assessed the influence of AvrPiz-t on CatB activity. AvrPiz-t greatly enhanced the efficiency of CatB-mediated H_2O_2 scavenging (Figure S7D). Moreover, expression of *AvrPiz-t* in rice led to increased catalase activity (Figure S7E), reduced H_2O_2 content (Figure S7F), and increased disease susceptibility (Figures S7G and S7H). Therefore, AvrPiz-t and ROD1 feed into the same ubiquitination-mediated protein degradation pathway and promote catalase-mediated ROS scavenging as an immune suppression strategy in host cells.

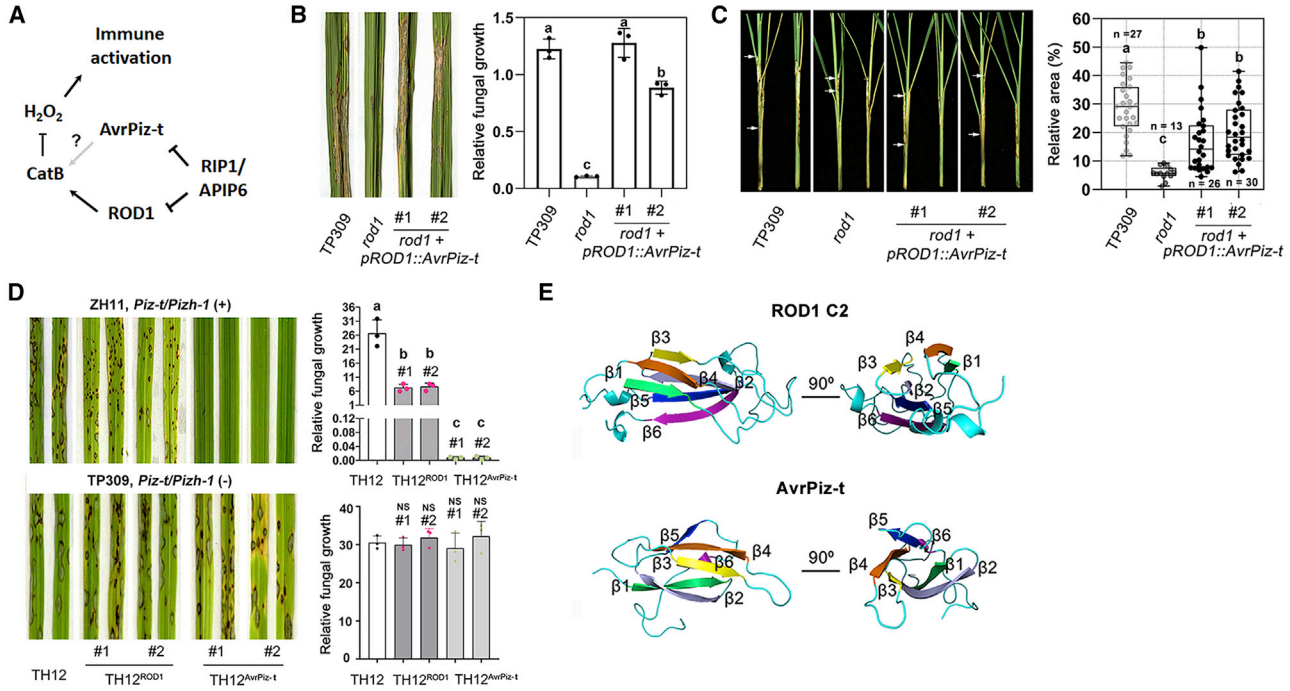

Figure 6. Structural mimicry and functional similarity between the blast pathogen effector AvrPiz-t and ROD1

(A) Schematic illustration showing the interplay between ROD1, RIP1/APIP6, and AvrPiz-t.

(B and C) *AvrPiz-t* expression largely compromised the *rod1* resistance to blast (B) (n = 3) and sheath blight (C). *AvrPiz-t* was expressed in the *rod1* plants using the *ROD1* promoter.

(D) Introduction of the $SP^{AvrPiz\text{-}t}$-*ROD1* chimera in the blast isolate TH12 ($TH12^{ROD1}$) that lacks *AvrPiz-t* partially rescued its avirulence in ZH11 containing the cognate *Piz-t* gene, when compared to the genetically complemented $TH12^{AvrPiz\text{-}t}$ isolate (upper panels). $TH12^{ROD1}$ did not change virulence in the susceptible variety TP309 (lower panels), indicating no increased basal defense to this transformant (n = 3).

(E) 3D structures and sequence comparison of the ROD1 C2 domain and AvrPiz-t. The homology model of ROD1 is derived based on the crystal structure of the Ca^{2+}-bound form of Munc13 C2B domain (PDB: 6NYT) (Shin et al., 2010). The AvrPiz-t structure has been solved (Zhang et al., 2013). Both proteins contain six β strands and exhibit a similar anti-parallel β sheet structure as illustrated by the PyMol Molecular Graphics System (version 2.0; Schrödinger).

Error bars in (B) and (D) represent mean ± SD, in (C) represent maximum and minimum values. Center line, median; box limits, 25th and 75th percentiles. Significant differences were determined by Duncan's new multiple range test and indicated with different letters. NS, not significant.

See also Figure S7.

To further investigate the functional relevance of the similarity between AvrPiz-t and ROD1, we performed mutual genetic complementation assays in rice and in the pathogen. *AvrPiz-t* was expressed in *rod1* plants under the control of the *ROD1* promoter. The *pROD1::AvrPiz-t* chimera largely suppressed the disease resistance phenotypes seen in *rod1* (Figures 6B and 6C). As a control, another rice blast fungal effector, AvrPik, which does not interact with APIP6, RIP1, or CatB, was tested. AvrPik expression had no effect on *rod1* disease resistance (Figures S7I and S7J), suggesting that AvrPiz-t specifically acts on the ROD1-mediated immune suppression circuit. We next explored whether ROD1 can substitute for AvrPiz-t function in pathogen virulence. TH12 is a *M. oryzae* strain with a loss-of-function allele of *AvrPiz-t*, which thus becomes virulent in the variety ZH11 carrying the cognate NLR gene *Piz-t*/*Pizh-1* (Xie et al., 2019). We found that ectopic expression of $SP^{AvrPiz\text{-}t}$-ROD1 (a chimeric protein composed of AvrPiz-t signal peptide and ROD1) in TH12 ($TH12^{ROD1}$) partially restored the avirulence in comparison with $TH12^{AvrPiz\text{-}t}$, leading to smaller and restricted lesions in ZH11 (Figure 6D). In contrast, the virulence of TH12 in TP309, a rice variety that lacks *Piz-t*, was not changed by ROD1expression (Figure 6D). These results suggest that pathogen-produced $SP^{AvrPiz\text{-}t}$-ROD1 converts TH12 into a partially avirulent strain and activates immunity in the presence of host Piz-t.

The above results demonstrate that ROD1 and AvrPiz-t share a common signaling module in host cells. In addition, although its' Ca^{2+} binding activity was very weak (Figure S7K), AvrPiz-t was also found to associate with phosphoinositide lipids such as PI(5)P and PI(3,5)P2, similar to ROD1 (Figure S7L). The interplay between ROD1 and AvrPiz-t is reminiscent of the functional or structural mimicry between mammalian and bacterial proteins (Elde and Malik, 2009). AvrPiz-t belongs to the MAX effector family, members of which have a conserved six β strand sandwich structure; however, little is known about the virulence mechanisms and targets of MAX effectors in plant hosts (de Guillen et al., 2015; Maqbool et al., 2015; Nyarko et al., 2014; Zhang et al., 2013). This anti-parallel β sandwich structure also exists in C2 domains from diverse organisms (SMART: SM00239). Using homology modeling, we found that, similarly to AvrPiz-t, the ROD1 C2 domain consists of six β strands that are organized

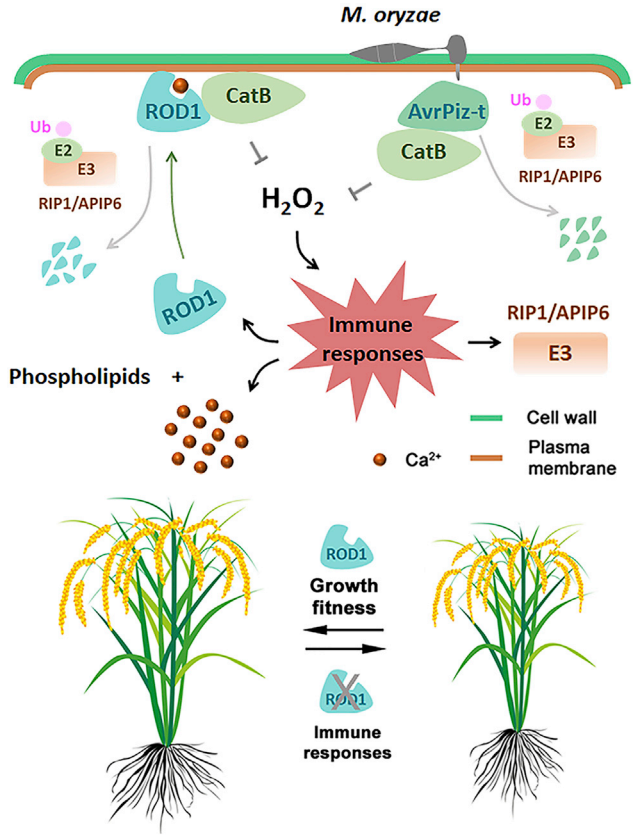

Figure 7. A proposed model for ROD1-mediated control of immune responses

Ca^{2+}-mediated ROD1 plasma membrane tethering initiates a signaling cascade that equilibrates immunity and growth fitness. Under normal conditions with low biotic stress, ROD1 recruits and stimulates CatB activity to eliminate H_2O_2 at the cell periphery, which restricts immunity and promotes plant growth. Upon pathogen infection, ROD1-CatB is further activated through the induction of ROD1 expression to buffer the immunity-triggered ROS burst. A pair of E3 ligases, RIP1 and APIP6, are induced to degrade ROD1 and thus rewire the ROD1 signaling circuit toward active immune responses. Both gene expression and protein localization dynamics of the "RIP1/APIP6-ROD1-CatB" module fine-tune immune activation, ensuring a balance between defense and plant growth. When ROD1 functions are deprived, plants constitutively activate immune responses that confer broad-spectrum resistance to multiple pathogens at the expense of growth. ROD1 protein surveillance with ubiquitination-mediated degradation and ROS scavenging function are exploited by the *M. oryzae* MAX effector AvrPiz-t, which can execute similar ROD1 function on immune suppression in rice cells, revealing a previously unrecognized mechanism of host-pathogen functional commonality on plant immune regulation.

into an anti-parallel β sandwich (Figure 6E). Given that protein function is largely determined by 3D conformation, the structural mimicry between ROD1 and AvrPiz-t may contribute to their functional convergence on the same immune suppression machinery.

DISCUSSION

Plants are challenged by numerous pathogens in their natural habitats thus must maintain an efficient, dynamic, and hierarchical immune system (Jones and Dangl, 2006). Because immune activation imposes trade-offs on plant growth, a delicate balance between warding off potential pathogens and avoiding negative impacts on growth fitness must be maintained. This is particularly important for cereal crops, which have been subjected to extensive domesticated selection of traits including high grain yield and reliable diseases resistance (Huang et al., 2010; Chen et al., 2019). However, it remains unclear how the balance between immunity and growth is coordinated in crops. Here, we have shown that the Ca^{2+}-binding protein ROD1 defines a specific immune circuit that integrates Ca^{2+}-sensing, ROS metabolism, and ubiquitination-mediated protein degradation to fine-tune immune responses and balance the conflict between defense and growth. By regulating ROS-scavenging-mediated immune suppression, ROD1 equilibrates immunity and growth fitness under normal conditions. Upon pathogen infection, ROD1-CatB is activated to buffer the immunity-triggered ROS burst. Pathogen infection also induces two E3 ligases, RIP1 and APIP6, which promote ROD1 degradation to sustain ROS production, thus ensuring reliable immune activation in the face of disease (Figure 7).

Functional mimicry has been observed in different pathogens. For example, a wild species of wheat has adopted a fungal glutathione S-transferase (GST) gene through horizontal gene transfer to deploy resistance against *Fusarium* head blight (Wang et al., 2020). We show that the pathogen effector AvrPiz-t structurally mimics ROD1 and both AvrPiz-t and ROD1 can stimulate CatB activity to degrade H_2O_2. Therefore, our study provides an example of cross-kingdom convergence on the regulation of ROS homeostasis, an additional arena in the arms race between plants and pathogens. Further investigations will reveal whether similar structural mimicry is deployed in other pathosystems.

Ca^{2+} is a prominent second messenger that mediates plant responses to abiotic and biotic stimuli (Dodd et al., 2010). During plant immune responses, elevated cytosolic Ca^{2+} signals are perceived and decoded by Ca^{2+} sensor proteins such as calcium-dependent protein kinases (CDPKs or CPKs), which, together with the PRR-associated kinase BIK1, phosphorylate the NADPH oxidase RBOHD to stimulate ROS production (Dubiella et al., 2013; Kadota et al., 2014; Li et al., 2014). Belonging to another class of Ca^{2+} sensors, ROD1 directly interacts with catalase and enhances its H_2O_2 scavenging activity. The Ca^{2+}-ROD1-CatB cascade may antagonize a Ca^{2+}-elicited ROS burst thus maintaining immune homeostasis (Yuan et al., 2017b). Immunity-triggered ROS accumulates mainly in the apoplastic space and has been proposed to be inhibited by pathogens (Guo et al., 2019; Hemetsberger et al., 2012; Qi et al., 2017). The punctate pattern of ROD1 in the PM, and the recruitment of CatB to the PM, would constitutes a shortcut that enables spatiotemporal precision in ROS degradation. Structural analysis may resolve the molecular basis of the ROD1-CatB complex functioning as an immune suppression hub.

Disease resistance and grain yield are the two major targets of rice breeding (Huang et al., 2010; Chen et al., 2019). Increased seed production of *rod1* in the blast nursey, as compared to the parent variety, suggests that pathogen resistance conferred by the *rod1* mutation outweighs the negative effect on growth during a disease outbreak. Intriguingly, we have identified a

natural variant of *ROD1* that increases field disease resistance without influencing other agronomic traits. This resistant allele, *ROD1* ($SNP1^A$), attenuates the activation of CatB-mediated ROS scavenging. *ROD1* ($SNP1^A$) is mainly distributed in low-latitude areas and enriched in *indica* rice varieties. This correlates with the wide cultivation of *indica* rice in tropical and subtropical regions (Huang et al., 2012), indicating differential defense strategies adopted in rice subspecies (Liao et al., 2016; Vergne et al., 2010). Given that pathogenic microbes have shaped plant defense and diversity (Delaux and Schornack, 2021), and that high temperature and humidity tends to benefit pathogen spreading (Beattie, 2011; Xin et al., 2016), the latitude-dependent distribution of *ROD1*($SNP1^A$) likely reflects an adaptation to high pathogen pressure, for example by *R. solani*, caused by local climate and agroecological conditions. Our data therefore argue that the selection of immune alleles through local adaptation is likely associated with specific agroecology. As elite rice varieties containing *ROD1*($SNP1^A$) exhibit higher field resistance without an obvious penalty in yield, *ROD1* may represent an elite target in crop breeding for high yield and broad-spectrum disease resistance.

Limitations of study

We show that the host protein ROD1 and the fungal pathogen effector AvrPiz-t converge on ROS scavenging-mediated immune suppression. However, it is unclear how ROD1 and AvrPiz-t promote catalase activity biochemically. The future challenge will be to determine the structural and biochemical features of the ROD1- and AvrPiz-t-CatB complexes. Another limitation of the study is with ROD1-mediated calcium signaling. Although it is clear that ROD1 binds and senses calcium, whether ROD1 regulates calcium signaling that is involved in immune responses will require future studies.

STAR★METHODS

Detailed methods are provided in the online version of this paper and include the following:

SUPPLEMENTAL INFORMATION

Supplemental information can be found online at https://doi.org/10.1016/j.cell.2021.09.009.

ACKNOWLEDGMENTS

We would like to thank Drs. Jane Parker, Sheng Yang He, Jianmin Zhou, and Xuehui Huang for critical reading and discussion; Drs. Bin Han and Xuehui Huang for help in genome sequence analysis; Dr. Yaling Wang for help in the isolation of *rod1*; Dr. Wanggen Zhang for maize transformation; Xin Wang for rice transformation; Drs. Jiachang Wang and Yongfei Wang for help with Ca^{2+} signaling; Dr. Wei Qian and Ms. Yao Wu for assistance in MST assay; and Mr. Qun Li, Xiaoyan Xu, and Yining Liu for assistance in SA and JA assay. This work was supported by the National Natural Science Foundation of China (32088102, 31930090, and 31720103913 to Z.H. and 31801718 to X.Y.), the Chinese Academy of Sciences Strategic Priority Research Program (XDB27040201 to Z.H. and XDB27030107 to W.Y.), the National Key Research and Development Program of China (2016YFD0100600), the Sino-German Center for Research Promotion (M-0275), and the Science and Technology Commission of Shanghai Municipality (19391900300). X.Y. was supported by the China Postdoctoral Science Foundation (2019M650036). X.Z. was supported by the National Postdoctoral Program for Innovative Talents (BX201700269) and the China Postdoctoral Science Foundation (2018M640425).

AUTHOR CONTRIBUTIONS

W.Y., X.Z., and Z.H. conceived the project. M.G., X.Y., X.Z., Y. He, B.Y., J.C., K.Z., Y.W., S.X., X.L., J.L., and J.Y. performed the experiments and analyzed the data. M.G., X.Y.., X.Z., Y. Huang, Y.D., G.Z., J.X., E.W., D.T., G.-L.,W., and Z.H. developed materials. H.C. and Y.D. performed the RNA-seq analysis. J.Y., W.Y., and X.G. performed the genome analysis. W.Y., M.G., and Z.H. wrote the paper. All authors discussed and commented on the manuscript.

DECLARATION OF INTERESTS

The authors declare no competing interests.

Received: March 11, 2021
Revised: July 23, 2021
Accepted: September 3, 2021
Published: September 30, 2021

REFERENCES

Bai, S., Liu, J., Chang, C., Zhang, L., Maekawa, T., Wang, Q., Xiao, W., Liu, Y., Chai, J., Takken, F.L., et al. (2012). Structure-function analysis of barley NLR immune receptor MLA10 reveals its cell compartment specific activity in cell death and disease resistance. PLoS Pathog. *8*, e1002752.

Barabaschi, D., Tondelli, A., Valè, G., and Cattivelli, L. (2020). Fitness cost shapes differential evolutionary dynamics of disease resistance genes in cultivated and wild plants. Mol. Plant *13*, 1352–1354.

Beattie, G.A. (2011). Water relations in the interaction of foliar bacterial pathogens with plants. Annu. Rev. Phytopathol. *49*, 533–555.

Boller, T., and Felix, G. (2009). A renaissance of elicitors: perception of microbe-associated molecular patterns and danger signals by pattern-recognition receptors. Annu. Rev. Plant Biol. *60*, 379–406.

Bomblies, K., Lempe, J., Epple, P., Warthmann, N., Lanz, C., Dangl, J.L., and Weigel, D. (2007). Autoimmune response as a mechanism for a Dobzhansky-Muller-type incompatibility syndrome in plants. PLoS Biol. *5*, e236.

Bonardi, V., Tang, S., Stallmann, A., Roberts, M., Cherkis, K., and Dangl, J.L. (2011). Expanded functions for a family of plant intracellular immune receptors beyond specific recognition of pathogen effectors. Proc. Natl. Acad. Sci. USA *108*, 16463–16468.

Brown, J.K. (2002). Yield penalties of disease resistance in crops. Curr. Opin. Plant Biol. *5*, 339–344.

Chen, Z., Silva, H., and Klessig, D.F. (1993). Active oxygen species in the induction of plant systemic acquired resistance by salicylic acid. Science *262*, 1883–1886.

Chen, E., Huang, X., Tian, Z., Wing, R.A., and Han, B. (2019). The genomics of *Oryza* species provides insights into rice domestication and heterosis. Annu. Rev. Plant Biol. *70*, 639–665.

Clapham, D.E. (2007). Calcium signaling. Cell *131*, 1047–1058.

Conrath, U., Beckers, G.J., Langenbach, C.J., and Jaskiewicz, M.R. (2015). Priming for enhanced defense. Annu. Rev. Phytopathol. *53*, 97–119.

de Guillen, K., Ortiz-Vallejo, D., Gracy, J., Fournier, E., Kroj, T., and Padilla, A. (2015). Structure analysis uncovers a highly diverse but structurally conserved effector family in phytopathogenic fungi. PLoS Pathog. *11*, e1005228.

Delaux, P.M., and Schornack, S. (2021). Plant evolution driven by interactions with symbiotic and pathogenic microbes. Science *371*, eaba6605.

Deng, Y., Zhai, K., Xie, Z., Yang, D., Zhu, X., Liu, J., Wang, X., Qin, P., Yang, Y., Zhang, G., et al. (2017). Epigenetic regulation of antagonistic receptors confers rice blast resistance with yield balance. Science *355*, 962–965.

Deng, Y., Ning, Y., Yang, D.L., Zhai, K., Wang, G.L., and He, Z. (2020). Molecular basis of disease resistance and perspectives on breeding strategies for resistance improvement in crops. Mol. Plant *13*, 1402–1419.

Dietrich, R.A., Richberg, M.H., Schmidt, R., Dean, C., and Dangl, J.L. (1997). A novel zinc finger protein is encoded by the Arabidopsis *LSD1* gene and functions as a negative regulator of plant cell death. Cell *88*, 685–694.

Dodd, A.N., Kudla, J., and Sanders, D. (2010). The language of calcium signaling. Annu. Rev. Plant Biol. *61*, 593–620.

Du, L., Ali, G.S., Simons, K.A., Hou, J., Yang, T., Reddy, A.S.N., and Poovaiah, B.W. (2009). $Ca^{(2+)}$/calmodulin regulates salicylic-acid-mediated plant immunity. Nature *457*, 1154–1158.

Dubiella, U., Seybold, H., Durian, G., Komander, E., Lassig, R., Witte, C.P., Schulze, W.X., and Romeis, T. (2013). Calcium-dependent protein kinase/NADPH oxidase activation circuit is required for rapid defense signal propagation. Proc. Natl. Acad. Sci. USA *110*, 8744–8749.

Elde, N.C., and Malik, H.S. (2009). The evolutionary conundrum of pathogen mimicry. Nat. Rev. Microbiol. *7*, 787–797.

Frye, C.A., Tang, D., and Innes, R.W. (2001). Negative regulation of defense responses in plants by a conserved MAPKK kinase. Proc. Natl. Acad. Sci. USA *98*, 373–378.

Gao, M., Yin, X., Yang, W., Lam, S.M., Tong, X., Liu, J., Wang, X., Li, Q., Shui, G., and He, Z. (2017). GDSL lipases modulate immunity through lipid homeostasis in rice. PLoS Pathog. *13*, e1006724.

Goodspeed, D., Chehab, E.W., Min-Venditti, A., Braam, J., and Covington, M.F. (2012). Arabidopsis synchronizes jasmonate-mediated defense with insect circadian behavior. Proc. Natl. Acad. Sci. USA *109*, 4674–4677.

Guo, Y., Yao, S., Yuan, T., Wang, Y., Zhang, D., and Tang, W. (2019). The spatiotemporal control of KatG2 catalase-peroxidase contributes to the invasiveness of *Fusarium graminearum* in host plants. Mol. Plant Pathol. *20*, 685–700.

Hemetsberger, C., Herrberger, C., Zechmann, B., Hillmer, M., and Doehlemann, G. (2012). The *Ustilago maydis* effector Pep1 suppresses plant immunity by inhibition of host peroxidase activity. PLoS Pathog. *8*, e1002684.

Huang, X., Wei, X., Sang, T., Zhao, Q., Feng, Q., Zhao, Y., Li, C., Zhu, C., Lu, T., Zhang, Z., et al. (2010). Genome-wide association studies of 14 agronomic traits in rice landraces. Nat. Genet. *42*, 961–967.

Huang, X., Kurata, N., Wei, X., Wang, Z.X., Wang, A., Zhao, Q., Zhao, Y., Liu, K., Lu, H., Li, W., et al. (2012). A map of rice genome variation reveals the origin of cultivated rice. Nature *490*, 497–501.

Huot, B., Yao, J., Montgomery, B.L., and He, S.Y. (2014). Growth-defense tradeoffs in plants: a balancing act to optimize fitness. Mol. Plant *7*, 1267–1287.

Jones, J.D., and Dangl, J.L. (2006). The plant immune system. Nature *444*, 323–329.

Kadota, Y., Sklenar, J., Derbyshire, P., Stransfeld, L., Asai, S., Ntoukakis, V., Jones, J.D., Shirasu, K., Menke, F., Jones, A., and Zipfel, C. (2014). Direct regulation of the NADPH oxidase RBOHD by the PRR-associated kinase BIK1 during plant immunity. Mol. Cell *54*, 43–55.

Kawano, Y., Akamatsu, A., Hayashi, K., Housen, Y., Okuda, J., Yao, A., Nakashima, A., Takahashi, H., Yoshida, H., Wong, H.L., et al. (2010). Activation of a Rac GTPase by the NLR family disease resistance protein Pit plays a critical role in rice innate immunity. Cell Host Microbe *7*, 362–375.

Kim, M.C., Panstruga, R., Elliott, C., Müller, J., Devoto, A., Yoon, H.W., Park, H.C., Cho, M.J., and Schulze-Lefert, P. (2002). Calmodulin interacts with MLO protein to regulate defence against mildew in barley. Nature *416*, 447–451.

Kumar, S., Stecher, G., and Tamura, K. (2016). MEGA7: Molecular Evolutionary Genetics Analysis version 7.0 for bigger datasets. Mol. Biol. Evol. *33*, 1870–1874.

Larkin, M.A., Blackshields, G., Brown, N.P., Chenna, R., McGettigan, P.A., McWilliam, H., Valentin, F., Wallace, I.M., Wilm, A., Lopez, R., et al. (2007). Clustal W and Clustal X version 2.0. Bioinformatics *23*, 2947–2948.

Li, L., Li, M., Yu, L., Zhou, Z., Liang, X., Liu, Z., Cai, G., Gao, L., Zhang, X., Wang, Y., Chen, S., and Zhou, J.M. (2014). The FLS2-associated kinase BIK1 directly phosphorylates the NADPH oxidase RbohD to control plant immunity. Cell Host Microbe *15*, 329–338.

Liao, J., Huang, H., Meusnier, I., Adreit, H., Ducasse, A., Bonnot, F., Pan, L., He, X., Kroj, T., Fournier, E., et al. (2016). Pathogen effectors and plant immunity determine specialization of the blast fungus to rice subspecies. eLife *5*, e19377.

Lolle, S., Greeff, C., Petersen, K., Roux, M., Jensen, M.K., Bressendorff, S., Rodriguez, E., Sømark, K., Mundy, J., and Petersen, M. (2017). Matching NLR immune receptors to autoimmunity in *camta3* mutants using antimorphic NLR alleles. Cell Host Microbe *21*, 518–529.e4.

Lopez, V.A., Park, B.C., Nowak, D., Sreelatha, A., Zembek, P., Fernandez, J., Servage, K.A., Gradowski, M., Hennig, J., Tomchick, D.R., et al. (2019). A bacterial effector mimics a host HSP90 client to undermine immunity. Cell *179*, 205–218.e21.

Ma, X., Zhang, Q., Zhu, Q., Liu, W., Chen, Y., Qiu, R., Wang, B., Yang, Z., Li, H., Lin, Y., et al. (2015). A robust CRISPR/Cas9 system for convenient, high-efficiency multiplex genome editing in monocot and dicot plants. Mol. Plant *8*, 1274–1284.

Macho, A.P., and Zipfel, C. (2014). Plant PRRs and the activation of innate immune signaling. Mol. Cell *54*, 263–272.

Maqbool, A., Saitoh, H., Franceschetti, M., Stevenson, C.E.M., Uemura, A., Kanzaki, H., Kamoun, S., Terauchi, R., and Banfield, M.J. (2015). Structural basis of pathogen recognition by an integrated HMA domain in a plant NLR immune receptor. eLife *4*, e08709.

Medina-Puche, L., Tan, H., Dogra, V., Wu, M., Rosas-Diaz, T., Wang, L., Ding, X., Zhang, D., Fu, X., Kim, C., and Lozano-Duran, R. (2020). A defense pathway linking plasma membrane and chloroplasts and co-opted by pathogens. Cell *182*, 1109–1124.e25.

Murray, D., and Honig, B. (2002). Electrostatic control of the membrane targeting of C2 domains. Mol. Cell *9*, 145–154.

Ning, Y., Liu, W., and Wang, G.L. (2017). Balancing immunity and yield in crop plants. Trends Plant Sci. *22*, 1069–1079.

Nobori, T., and Tsuda, K. (2019). The plant immune system in heterogeneous environments. Curr. Opin. Plant Biol. *50*, 58–66.

Nyarko, A., Singarapu, K.K., Figueroa, M., Manning, V.A., Pandelova, I., Wolpert, T.J., Ciuffetti, L.M., and Barbar, E. (2014). Solution NMR structures of *Pyrenophora tritici-repentis* ToxB and its inactive homolog reveal potential determinants of toxin activity. J. Biol. Chem. *289*, 25946–25956.

Okazaki, K., Miyagishima, S.Y., and Wada, H. (2015). Phosphatidylinositol 4-phosphate negatively regulates chloroplast division in Arabidopsis. Plant Cell *27*, 663–674.

Park, C.H., Chen, S., Shirsekar, G., Zhou, B., Khang, C.H., Songkumarn, P., Afzal, A.J., Ning, Y., Wang, R., Bellizzi, M., et al. (2012). The *Magnaporthe oryzae* effector AvrPiz-t targets the RING E3 ubiquitin ligase APIP6 to suppress pathogen-associated molecular pattern-triggered immunity in rice. Plant Cell *24*, 4748–4762.

Qi, J., Wang, J., Gong, Z., and Zhou, J.M. (2017). Apoplastic ROS signaling in plant immunity. Curr. Opin. Plant Biol. *38*, 92–100.

Rizo, J., and Südhof, T.C. (1998). C2-domains, structure and function of a universal Ca^{2+}-binding domain. J. Biol. Chem. *273*, 15879–15882.

Shin, O.H., Lu, J., Rhee, J.S., Tomchick, D.R., Pang, Z.P., Wojcik, S.M., Camacho-Perez, M., Brose, N., Machius, M., Rizo, J., et al. (2010). Munc13 C2B domain is an activity-dependent Ca^{2+} regulator of synaptic exocytosis. Nat. Struct. Mol. Biol. *17*, 280–288.

Spoel, S.H., and Dong, X. (2012). How do plants achieve immunity? Defence without specialized immune cells. Nat. Rev. Immunol. *12*, 89–100.

Talbot, N.J., Ebbole, D.J., and Hamer, J.E. (1993). Identification and characterization of MPG1, a gene involved in pathogenicity from the rice blast fungus Magnaporthe grisea. Plant Cell *5*, 1575–1590.

Tian, D., Traw, M.B., Chen, J.Q., Kreitman, M., and Bergelson, J. (2003). Fitness costs of R-gene-mediated resistance in *Arabidopsis thaliana*. Nature *423*, 74–77.

Todesco, M., Balasubramanian, S., Hu, T.T., Traw, M.B., Horton, M., Epple, P., Kuhns, C., Sureshkumar, S., Schwartz, C., Lanz, C., et al. (2010). Natural allelic variation underlying a major fitness trade-off in *Arabidopsis thaliana*. Nature *465*, 632–636.

Upson, J.L., Zess, E.K., Białas, A., Wu, C.H., and Kamoun, S. (2018). The coming of age of EvoMPMI: evolutionary molecular plant-microbe interactions across multiple timescales. Curr. Opin. Plant Biol. *44*, 108–116.

van Schie, C.C., and Takken, F.L. (2014). Susceptibility genes 101: how to be a good host. Annu. Rev. Phytopathol. *52*, 551–581.

Vergne, E., Grand, X., Ballini, E., Chalvon, V., Saindrenan, P., Tharreau, D., Nottéghem, J.-L., and Morel, J.-B. (2010). Preformed expression of defense is a hallmark of partial resistance to rice blast fungal pathogen *Magnaporthe oryzae*. BMC Plant Biol. *10*, 206.

Wang, W., Barnaby, J.Y., Tada, Y., Li, H., Tör, M., Caldelari, D., Lee, D.U., Fu, X.D., and Dong, X. (2011). Timing of plant immune responses by a central circadian regulator. Nature *470*, 110–114.

Wang, W., Mauleon, R., Hu, Z., Chebotarov, D., Tai, S., Wu, Z., Li, M., Zheng, T., Fuentes, R.R., Zhang, F., et al. (2018). Genomic variation in 3,010 diverse accessions of Asian cultivated rice. Nature *557*, 43–49.

Wang, H., Sun, S., Ge, W., Zhao, L., Hou, B., Wang, K., Lyu, Z., Chen, L., Xu, S., Guo, J., et al. (2020). Horizontal gene transfer of *Fhb7* from fungus underlies *Fusarium* head blight resistance in wheat. Science *368*, eaba5435.

Waszczak, C., Carmody, M., and Kangasjärvi, J. (2018). Reactive oxygen species in plant signaling. Annu. Rev. Plant Biol. *69*, 209–236.

Weydert, C.J., and Cullen, J.J. (2010). Measurement of superoxide dismutase, catalase and glutathione peroxidase in cultured cells and tissue. Nat. Protoc. *5*, 51–66.

Xie, Z., Yan, B., Shou, J., Tang, J., Wang, X., Zhai, K., Liu, J., Li, Q., Luo, M., Deng, Y., and He, Z. (2019). A nucleotide-binding site-leucine-rich repeat receptor pair confers broad-spectrum disease resistance through physical association in rice. Philos. Trans. R. Soc. Lond. B Biol. Sci. *374*, 20180308.

Xin, X.F., Nomura, K., Aung, K., Velásquez, A.C., Yao, J., Boutrot, F., Chang, J.H., Zipfel, C., and He, S.Y. (2016). Bacteria establish an aqueous living space in plants crucial for virulence. Nature *539*, 524–529.

Yang, W., Wightman, R., and Meyerowitz, E.M. (2017). Cell cycle control by nuclear sequestration of CDC20 and CDH1 mRNA in plant stem cells. Mol. Cell *68*, 1108–1119.e3.

Yang, Z., Wang, C., Xue, Y., Liu, X., Chen, S., Song, C., Yang, Y., and Guo, Y. (2019). Calcium-activated 14-3-3 proteins as a molecular switch in salt stress tolerance. Nat. Commun. *10*, 1199.

Yin, X., Zou, B., Hong, X., Gao, M., Yang, W., Zhong, X., He, Y., Kuai, P., Lou, Y., Huang, J., et al. (2018). Rice copine genes OsBON1 and OsBON3 function as suppressors of broad-spectrum disease resistance. Plant Biotechnol. J. *16*, 1476–1487.

You, Q., Zhai, K., Yang, D., Yang, W., Wu, J., Liu, J., Pan, W., Wang, J., Zhu, X., Jian, Y., et al. (2016). An E3 ubiquitin ligase-BAG protein module controls plant innate immunity and broad-spectrum disease resistance. Cell Host Microbe *20*, 758–769.

Yuan, H.M., Liu, W.C., and Lu, Y.T. (2017a). CATALASE2 coordinates SA-mediated repression of both auxin accumulation and JA biosynthesis in plant defenses. Cell Host Microbe *21*, 143–155.

Yuan, P., Jauregui, E., Du, L., Tanaka, K., and Poovaiah, B.W. (2017b). Calcium signatures and signaling events orchestrate plant-microbe interactions. Curr. Opin. Plant Biol. *38*, 173–183.

Zhai, K., Deng, Y., Liang, D., Tang, J., Liu, J., Yan, B., Yin, X., Lin, H., Chen, F., Yang, D., et al. (2019). RRM transcription factors interact with NLRs and regulate broad-spectrum blast resistance in rice. Mol. Cell *74*, 996–1009.e7.

Zhang, H.K., Zhang, X., Mao, B.Z., Li, Q., and He, Z.H. (2004). Alpha-picolinic acid, a fungal toxin and mammal apoptosis-inducing agent, elicits hypersensitive-like response and enhances disease resistance in rice. Cell Res. *14*, 27–33.

Zhang, Z.M., Zhang, X., Zhou, Z.R., Hu, H.Y., Liu, M., Zhou, B., and Zhou, J. (2013). Solution structure of the *Magnaporthe oryzae* avirulence protein AvrPiz-t. J. Biomol. NMR *55*, 219–223.

Zhang, Z., Xu, Y., Xie, Z., Li, X., He, Z.H., and Peng, X.X. (2016). Association-dissociation of glycolate oxidase with catalase in rice: a potential switch to modulate intracellular H_2O_2 levels. Mol. Plant *9*, 737–748.

Zhou, M., Wang, W., Karapetyan, S., Mwimba, M., Marqués, J., Buchler, N.E., and Dong, X. (2015). Redox rhythm reinforces the circadian clock to gate immune response. Nature *523*, 472–476.

Zhou, Y.B., Liu, C., Tang, D.Y., Yan, L., Wang, D., Yang, Y.Z., Gui, J.S., Zhao, X.Y., Li, L.G., Tang, X.D., et al. (2018). The receptor-like cytoplasmic kinase STRK1 phosphorylates and activates CatC, thereby regulating H_2O_2 homeostasis and improving salt tolerance in rice. Plant Cell *30*, 1100–1118.

Zipfel, C., and Oldroyd, G.E. (2017). Plant signalling in symbiosis and immunity. Nature *543*, 328–336.

Zou, J.J., Li, X.D., Ratnasekera, D., Wang, C., Liu, W.X., Song, L.F., Zhang, W.Z., and Wu, W.H. (2015). Arabidopsis CALCIUM-DEPENDENT PROTEIN KINASE8 and CATALASE3 function in abscisic acid-mediated signaling and H_2O_2 homeostasis in stomatal guard cells under drought stress. Plant Cell *27*, 1445–1460.

STAR★METHODS

KEY RESOURCES TABLE

REAGENT or RESOURCE	SOURCE	IDENTIFIER
Antibodies		
Mouse monoclonal anti-ACTIN	CMCTAG	Cat# AT0004
Rabbit anti-ROD1	This paper	N/A
Mouse monoclonal anti-MYC	MILLIPORE	Cat# 05-724; RRID: AB_11211891
Rabbit monoclonal anti-GFP	Abcam	Cat# ab32146; RRID:AB_732717
Mouse monoclonal I anti-GFP	Abcam	Cat# ab1218; RRID:AB_298911
Mouse monoclonal anti-MBP HRP conjugate	NEB	Cat# E8038S; RRID: AB_1559738
Mouse monoclonal anti-GST	CMCTAG	Cat# CW0291
Mouse monoclonal anti-Ubiquitin	CST	Cat #3936; RRID: AB_331292
Rabbit Polyclonal anti-FLAG	Proteintech	Cat 20543-1-AP; RRID:AB_11232216
Goat anti-Rabbit IgG Secondary Antibody, HRP conjugate	Thermo Fisher	Cat# 31460; RRID: AB_228341
Goat anti-mouse IgG Secondary Antibody, HRP conjugate	CWBIO	Cat# CW0102; RRID:AB_2736997
Bacterial and fungal strains		
Magnaporthe oryzae TH12	This paper	N/A
Magnaporthe oryzae $SP^{AvrPiz\text{-}t}$-ROD1/TH12	This paper	N/A
Magnaporthe oryzae $SP^{AvrPiz\text{-}t}$-AvrPiz-t/TH12	This paper	N/A
Escherichia coli DH5a	Weidi Biotechnology	Cat#DL1001
Escherichia coli Rosetta (DE3)	Weidi Biotechnology	Cat#EC1010
Agrobacterium tumefaciens strain GV3101	Weidi Biotechnology	Cat#AC1001
Agrobacterium tumefaciens strain EHA105	Weidi Biotechnology	Cat#AC1010
Saccharomyces cerevisiae strain AH109	Weidi Biotechnology	Cat#YC1010
Rhizoctonia solani AG1-IA (isolate RH-9)	This paper	N/A
Xanthomonas oryzae pv. oryzae PXO99A	This paper	N/A
Chemicals, peptides, and recombinant proteins		
TRIzol Reagent	Invitrogen	Cat#15596018
ReverTra Ace qPCR RT Master Mix with gDNA Remover	TOYOBO	Cat#FSQ-301
SuperScript III First-Strand Synthesis SuperMix	Invitrogen	Cat#18080400
SYBR Premix Ex Taq	Takara	Cat#RR420A
Macerozyme R-10	Yakult Pharmaceutical	CAS: 9032-75-1
Cellulase R-10	Yakult Pharmaceutical	CAS: 9012-54-8
3-amino-1,2,4-triazole	Sigma-Aldrich	Cat#A8056
DO Supplement -Leu/-Trp	Clontech	Cat#630417
DO Supplement -His/-Leu/-Trp	Clontech	Cat#630419
DO Supplement -His/-Leu/-Trp/-Ade	Clontech	Cat#630428
Lipid strips	Echelon Biosciences	P-6001
Critical commercial assays		
Catalase assay	Beyotime	Cat#S0051
Measurement of H_2O_2	Molecular Probes	Amplex Red hydrogen peroxide assay kit
Luciferase Assay	Promega	Cat#E1501
Anti-GFP (Green Fluorescent Protein) mAb-Magnetic Agarose	MBL	D153-10
MYC Tag IP/Co-IP Kit	Thermo	Cat #88842
Anti-FLAG M2 Magnetic Beads	Sigma	M8823
pENTR/D-TOPO Cloning Kit	Invitrogen	Cat#45-0218
Gateway LR Clonase II Enzyme Mix	Invitrogen	Cat#11791-020

(*Continued on next page*)

Continued

REAGENT or RESOURCE	SOURCE	IDENTIFIER
HiSpeed Plasmid Midi Kit	QIAGEN	Cat#12643
ClonExpress II One Step Cloning Kit	Vazyme	Cat C112
Deposited data		
RNA-seq dataset	This paper	GSE167877
Experimental models: Organisms/strains		
Oryza sativa TP309, Zhonghua 11, *japonica*	This paper	N/A
Oryza sativa Taichung Native 1, *indica*	This paper	N/A
Oryza sativa Huajingxian 74, CSSL1, CSSL2, *indica*	This paper	N/A
Oryza sativa rod1, japonica	This paper	N/A
Rice: *pROD1::ROD1(SNP1^{C})/rod1*	This paper	N/A
Rice: *pROD1::ROD1(SNP1^{A})/rod1*	This paper	N/A
Rice: *pROD1::ROD1^{D72N}/rod1*	This paper	N/A
Rice: *pROD1::ROD1^{D1322N}/rod1*	This paper	N/A
Rice: *pROD1::ROD1$^{D\text{-}quad}$/rod1*	This paper	N/A
Rice: *pUbi::ROD1*/TP309	This paper	N/A
Rice: *pUbi::RIP1*/TP309	This paper	N/A
Rice: *pUbi:APIP6*/TP309	This paper	N/A
Rice: *RIP1*-KO/TP309	This paper	N/A
Rice: *APIP6*-KO/TP309	This paper	N/A
Rice: *pROD1:Avrpiz-t/rod1*	This paper	N/A
Rice: *pROD1:AvrPik/rod1*	This paper	N/A
Rice: *pUbi::Avrpiz-t*/TP309	This paper	N/A
Maize *CR-zmrod1*/C01	This paper	N/A
Nicotiana benthamiana	N/A	N/A
Recombinant DNA		
1300-pROD1::GUS	This paper	N/A
pUN1301-ROD1	This paper	N/A
pUN1301-AvrPiz-t	This paper	N/A
1300-pROD1::ROD1	This paper	N/A
1300-pROD1::ROD1A	This paper	N/A
1300-pROD1:: AvrPiz-t	This paper	N/A
CRISPR-RIP1	This paper	N/A
pUN1301-RIP1	This paper	N/A
CRISPR-APIP6	This paper	N/A
pUN1301-APIP6	This paper	N/A
CRISPR-ZmROD1	This paper	N/A
1300- pROD1::ROD1D72N	This paper	N/A
1300- pROD1::ROD1D132N	This paper	N/A
1300- pROD1::ROD1D-trip	This paper	N/A
1300- pROD1::ROD1D-quad	This paper	N/A
SP$^{AvrPiz\text{-}t}$-ROD1	This paper	N/A
MBP-RIP1	This paper	N/A
MBP-APIP6	This paper	N/A
MBP-RIP1 H74Y	This paper	N/A
MBP-APIP6 H58Y	This paper	N/A
pCOLD-ROD1A	This paper	N/A
pCOLD-ROD1	This paper	N/A

(*Continued on next page*)

Continued

REAGENT or RESOURCE	SOURCE	IDENTIFIER
pCOLD-ROD1quad	This paper	N/A
pENTR-ROD1	This paper	N/A
pDEST32-ROD1	This paper	N/A
pGBKT7-ROD1	This paper	N/A
pGADT7-ROD1	This paper	N/A
pGBKT7-APIP6	This paper	N/A
pGADT7-APIP6	This paper	N/A
pGBKT7-APIP6(ρ)	This paper	N/A
pGADT7-APIP6(ρ)	This paper	N/A
pGBKT7-RIP1	This paper	N/A
pGADT7-RIP1	This paper	N/A
pGBKT7-RIP1(ρ)	This paper	N/A
pGADT7-RIP1(ρ)	This paper	N/A
pGBKT7-CatB	This paper	N/A
pGADT7-CatB	This paper	N/A
pGBKT7-AvrPiz-t	This paper	N/A
pGADT7-AvrPiz-t	This paper	N/A
CatB-FLAG	This paper	N/A
ROD1-GFP	This paper	N/A
ROD1A-GFP	This paper	N/A
MLA10-HA	This paper	N/A
AvrPiz-t-MYC	This paper	N/A
APIP6(ρ)-MYC	This paper	N/A
RIP1(ρ)-MYC	This paper	N/A
YFP-CatB	This paper	N/A
mCherry-ROD1	This paper	N/A
nVenus-CatB	This paper	N/A
cCFP-ROD1	This paper	N/A
PigmR-CC-nLuc	This paper	N/A
PigmR-CC-FLAG	This paper	N/A
AvrPiz-t-TF	This paper	N/A
Software and algorithms		
ImageJ	NIH	https://imagej.net/software/fiji/
GraphPad Prism 7	GraphPad Software	https://www.graphpad.com/
Clustal X (1.83)	Larkin et al., 2007	http://www.clustal.org/clustal2/
MEGA7	Kumar et al., 2016	https://megasoftware.net/

RESOURCE AVAILABILITY

Lead contact

Further information and request for resources and reagents should be directed to and will be fulfilled by the Lead Contact, Zuhua He (zhhe@cemps.ac.cn).

Materials availability

Constructs, transgenic seeds and antibodies generated in this study will be made available upon request, but a completed Materials Transfer Agreement may be required if there is potential for commercial application.

Data and code availability

- **Data.** The RNA-seq data generated in this study have been deposited at the GEO database and are publicly available as of the date of publication. Accession number is listed in the Key resources table.
- **Code.** This paper does not report original code.
- **Additional information.** This study did not generate any additional information.

EXPERIMENTAL MODEL AND SUBJECT DETAILS

Plant materials and growth conditions

Rice varieties, including TP309 and *rod1* mutant (*japonica*), Taichung Native 1 (TN1, *indica*), and Zhonghua 11 (ZH11, *japonica*), were used in this study. All rice wild-type and transgenic plants were grown in protected paddy fields at the Shanghai or Hainan Island experimental stations. For experiments with seedlings, plants were grown in a growth chamber under the conditions of 12-h day, 28°C, 80% RH followed by 12-h night, 26°C, 60% RH.

Maize (*Zea mays*, accession C01) plants were grown in the greenhouse with temperature between 25°C and 32°C. Tobacco (*Nicotiana benthamiana*) plants were grown at 22°C under long-day conditions (16-h day/8-h night) and 3∼4 weeks old leaves were used for transient expression experiments.

Pathogens

The hemibiotrophic rice blast fungus *Magnarpothe oryzae* isolate TH12, the transformants TH12$^{AvrPiz\text{-}T}$ and TH12^{ROD1}, the hemibiotrophic bacterial blight pathogen *Xanthomonas oryzae* pv. *oryzae* (*Xoo*) Philippine strain P6 (PXO99A), and the necrotrophic sheath blight fungus *Rhizoctonia solani* (*R. solani*) AG1-IA (isolate RH-9) were used in this study.

METHOD DETAILS

Map-Based Cloning, Complementation, and Overexpression

The *rod1* allele was initially isolated from a TP309 (*japonica*) breeding population, which was crossed with TP309 to purify the background. The *rod1* mutant was crossed with TN1 (*indica*) to generate an F2 mapping population. *ROD1* was roughly delimited to an interval between two simple sequence repeat (SSR) markers RM587 and RM597 near the telomere of Chromosome 6. Due to a low recombination ratio in this region, a large mapping population was generated and ∼10,000 F_2 individuals were used for fine mapping. With newly developed InDel and CAPS markers, the *ROD1* locus was narrowed down to a 53-kb DNA region. There are seven open reading frames (ORFs) in this region. Genomic DNA fragments of this region were amplified from *rod1* and TP309 plants, sequenced, and compared using MegAlign (DNASTAR).

For complementation, genomic DNA containing the *ROD1* promoter as well its coding region was amplified and inserted into pCambia1300. The resulting construct 1300-pROD1::ROD1 was transformed into *rod1* calli via *Agrobacterium tumefaciens*-mediated transformation. More than 20 independent transgenic lines were produced that could successfully rescue the *rod1* mutant phenotypes.

1300-pROD1::ROD1 was also transformed into TP309 background, resulting in *ROD1* overexpression plants driven its native promoter. For *ROD1* overexpression driven by the maize *UBIQUTIN1* promoter, *ROD1* genomic region was inserted into the vector pUN1301. The resulting pUN1301-ROD1 construct was transformed into TP309 plants to produce more than 20 independent overexpression lines.

Construction of Transgenic Rice Plants

APIP6 and *RIP1* overexpression was driven by the maize *UBIQUTIN1* promoter, *APIP6* and *RIP1* cDNAs were inserted into the vector pUN1301. The resulting pUN1301-APIP6 and pUN1301-RIP1 constructs were transformed into TP309 and *rod1* plants to produce more than 15 independent overexpression lines.

For *CatB* overexpression driven by the maize *UBIQUTIN1* promoter, *CatB* cDNA fused with FLAG was inserted into the vector pUN1301. The resulting pUN1301-CatB-FLAG construct was transformed into TP309 and *rod1* plants to produce more than 15 independent overexpression lines.

ROD1^{A} was amplified from TN1 (*indica*) and inserted into the plasmid 1300-pROD1::ROD1 which was digested by BamHI and *Sac*I to generate 1300-pROD1::ROD1^{A}. The resulting construct 1300-pROD1::ROD1^{A} was transformed into the *rod1* background, to produce more than 20 independent transgenic lines. 1300-pROD1::AvrPiz-t and 1300-pROD1::AvrPik were transformed into the *rod1* background to produce more than 15 independent overexpression lines

CRISPR/Cas9 Mutation in Rice and Maize

For CRISPR/Cas9 mediated gene knockout mutation, two 20-bp gene-specific guide RNA sequences targeting *APIP6* or *RIP1* were synthesized, annealed, and ligated into pOs-sgRNA, which was subcloned into the vector pYLCRISPR/Cas9-MH (Ma et al., 2015). The constructs were transformed into TP309 *Agrobacterium tumefaciens*-mediated transformation. More than 15 independent lines were generated for each transformation. PCR-based sequencing was performed to verify the mutation sites of the target genes.

For CRISPR/Cas9 mediated gene knockout mutation in maize, two guide RNA sequences from the *ZmROD1* coding region were cloned into pYLCRISPR/Cas9-MH (Bar+) vector to generate the *ZmROD1* CRISPR/Cas9 construct. The resulting CRISPR/Cas9 plasmids were introduced into the maize accession C01 using *Agrobacterium tumefaciens*. Mutant lines were confirmed by PCR followed by sequencing.

Pathogen Inoculation Experiments

Blast fungal inoculation was conducted as previously described (Deng et al., 2017; Zhai et al., 2019). Briefly, *M. oryzae* (isolate TH12) was cultured on complete agar medium at 25°C for 10 days to produce spores. Leaves at tillering stage were punch-inoculated with spores diluted in distilled H_2O at a concentration of 1×10^5 spores/mL. For blast inoculation in seedlings, two-week-old plants were sprayed with blast spore suspensions. Inoculated seedlings were kept in a dew growth chamber at 26°C for 24 h in darkness, and then grown at 26°C with 12 h/12 h (day/night) and 90% relative humidity for 7 days. Lesion lengths were measured and fungal growth was determined using quantitative PCR (Kawano et al., 2010) to measure the amount of *Pot2* transposon DNA, which was normalized to the rice *ubiquitin* gene (*LOC_Os03 g13170*). PCR primers are listed in Table S3.

Sheath blight inoculation was carried out at tillering stages in the paddy field as previously reported with slight modification (Yin et al., 2018). Briefly, *Rhizoctonia solani* AG1-IA (isolate RH-9) was cultured on PDA (potato-dextrose-agar) plates for 2 d at 28°C. Short (0.8-1.0 cm) wooden toothpicks were sterilized and co-incubated with fungal plugs for 3 d at 28°C. The fungi growing toothpicks were then inserted into the third leaf sheath. Sheath blight symptom was recorded at 7 dpi with more than 20 sheaths each genotype (2 sheaths per plant) analyzed.

For the *Xoo* infection assay, bacterial strain PXO99A was grown on a peptone sucrose agar (PSA) medium at 28°C for 3 days. The bacteria were collected and then suspended in sterilized water at a concentration of OD600 = 1.0, which were used to infect two-month-old plants (tillering stage) by the leaf-clipping method (Gao et al., 2017). Lesion length was measured at 14 dpi. All fungal and bacterial infections were repeated independently at least three times.

Rice Blast Nursery Test

Field evaluation of rice blast resistance was performed as previously described (Deng et al., 2017). In brief, ~100 rice plants of each genotype were grown in the Donghui blast nursery (Zhejiang, China). Blast disease was recorded at tillering stage, and grain production was measured at mature stage. Plants grown in a neighbor non-diseased paddy field in the same mountain area were assayed as a control for grain production.

Ca^{2+} Binding Site Mutation and Complementation

To generate ROD1 Ca^{2+} binding site mutants, the mutation sites were introduced using primers. The plasmid SK-ROD1 containing *ROD1* coding sequence was used as a template for PCR-based mutagenesis. The PCR products were self-ligated. The SK-ROD1-D-doub was used as template to generate ROD1-D-trip by PCR. ROD-D-quad was generated by PCR using SK-ROD1-D-doub as template. All constructs were validated by sequencing. The resulting mutation constructs 1300-pROD1::ROD^{D72N}, 1300-pROD1::ROD^{D132N}, and 1300-pROD1::$ROD^{D\text{-}quad}$ were transformed into *rod1* calli. More than 15 independent transgenic lines were used for phenotypic analysis.

M. oryzae Transformation

For expression of *ROD1* in *M. oryzae* TH12 strain, *ROD1* coding sequence (using primers ROD1-CDS-PstI-F and ROD1-CDS-HindIII-R, Table S3) was fused with the signal peptide of AvrPiz-t (using primers Apt-1192-NotI-F and Apt-SP-PstI-R, Table S3). The coding sequences of *AvrPiz-t* was cloned into vector pBC1532 by PCR using primers (Table S3). *M. oryzae* transformation was performed as described previously (Talbot et al., 1993) with slight modifications. In details, a 3 cm^2 square of mycelium was macerated in 200-300 mL liquid media and incubated at 28°C for 48 h on a rotary shaker at 200 rpm. The mycelium was suspended in 2 mL of cell wall digestion solution [15 mg/ml Lysing Enzymes from *Trichoderma harzianum* (Sigma L1412), 25 mg/mL Driselase from *Basidiomycetes* sp. (Sigma D9515), 0.4 mg/mL chitinase from *Streptomyces griseus* (Sigma C6137), in 0.7M NaCl buffer (pH5.8)] at room temperature on a rotary shaker at 60 rpm for 3 h. The fungal protoplasts were filtered through 3 layers of Miracloth and harvested by centrifuge at 4,100 g for 10 min. The pellet was re-suspended in 10 mL of STC buffer (1.2 M sorbitol, 10 mM Tris-HCl, pH 7.5, 20 mM $CaCl_2$). 150 μL protoplasts (1×10^8 cells/ml) were mixed with 2 μg DNA and incubated at room temperature for 25 min. After adding 1 mL PTC buffer (60% polyethylene glycol 4000, 10 mM Tris-HCl, pH 7.5, 20 mM $CaCl_2$), the mixture was incubated for another 25 min. Next, 5 mL of TB3 [0.3% Yeast Extract, 0.3% Casamina acids (sigma C7290), 20% Sucrose] was added, and the protoplasts were cultured for 12-18 h at 28°C. The protoplasts were poured onto 150-mm plates. A selective overlay of 0.75% TB3 agar containing 100 μg /mL HygB was added. After incubation at 30°C in the dark for 6 days, transformants were picked to CM plates and allowed to sporulate. Single conidia were then isolated from each transformant and confirmed by DNA sequencing.

Yeast Two Hybrid (Y2H) Screening and Protein Interaction

Y2H screening was carried out to identify ROD1 interacting proteins used a rice cDNA library developed from mRNAs prepared from rice seedling infected by rice blast as previously described (Zhai et al., 2019). Briefly, *ROD1* was amplified with primers F: CACCATGT CGGAGGCGATGTT and R: CGGGTTAGTCAACGTCTCG to generate target coding sequence, then a BP recombination reaction

was performed to generate *pENTR-ROD1* entry vector, and ROD1 protein was fused to the GAL4 DNA binding domain in vector pDEST32 using a LR recombination reaction (Invitrogen). The resulting construct was used as a bait to screen a cDNA library. For the Y2H assay, the coding sequences of *ROD1*, *APIP6*, *RIP1*, *CatB*, *AvrPiz-t* and *AvrPik* were amplified with gene specific primers (Table S3) and cloned into the yeast expression vectors pGADT7 and pGBKT7. The resulting constructs were co-transformed into yeast strain AH109. The yeast transformants were grown on nutrient-restricted mediums to assess interactions between various protein combinations.

Co-Immunoprecipitation (Co-IP)

To verify the protein interactions *in planta*, we carried out Co-IP assays. The *ROD1* coding sequence was amplified and cloned into the vector pCAMBIA1300-35S-eGFP(C)-rbcsE9. *APIP6 (Δ)* and *RIP1(Δ)* coding sequences were cloned into the vector pCAMBIA1300-35S-4Myc(C) to generate expression vectors. The *AvrPiz-t* (without signal peptide) coding sequence was fused into vector pCAMBIA1300-35S-Myc(C)-rbcsE9, the *CatB* coding sequence was amplified and fused into vector pCAMBIA1300-35S-Flag(C)-rbcsE9 to generate CatB-Flag. All plasmids were transformed into *Agrobacterium* (GV3101) and expressed in *N. benthamiana* leaves by co-infiltration. Infiltrated leaves were ground into powder in liquid nitrogen and homogenized in extraction buffer (50 mM Tris-HCl, pH 7.5, 150 mM NaCl, 0.5% Triton X-100, 5% glycerol, 2 mM EDTA, and 1% protease inhibitor cocktail). Supernatants were incubated with anti-GFP/MYC/FLAG beads for 4 h at 4°C and washed 5 times with the extraction buffer. Proteins were eluted from the beads by boiling in SDS loading buffer for 10 min. MYC-IP experiments were performed with the Pierce MYC Tag IP/Co-IP Kit (Thermo, #88842) following the manufacturer's instructions.

Split Luciferase Complementation

The coding sequences of *ROD1* and *CatB* were inserted into pCAMBIA-35S-nLuc and pCAMBIA-35S-cLuc, respectively. The resulting plasmids were transformed into *Agrobacterium* GV3101. After culture in LB media overnight at 28°C, the bacteria were collected and resuspended in infiltration buffer (10 mM $MgCl_2$, 10 mM MES,150 μM acetosyringone, pH 5.6), and incubated for 2∼3 hours at 30°C. The suspensions were infiltrated into leaves of three-week-old *N. benthamiana*. Luciferase activity was measured with Luciferase Assay Systems (Promega) after 2 days of transformation.

E3 Ligase Ubiquitination Assay

To assess E3 ubiquitin ligase activity of RIP1 and APIP6, and the ubiquitination of ROD1 by RIP1 and APIP6, we performed *in vitro* ubiquitination assays as previously described (Park et al., 2012; You et al., 2016). The *ROD1* coding sequence was inserted into vector pCold^{TM} TF (TaKaRa). APIP6, RIP1 and their mutated forms APIP6 (H58Y) and RIP1(H74Y) were cloned into pMAL-c5X. The fusion constructs were introduced into *E. coli* strain Rosetta (DE3) and grown in LB medium at 37°C to OD600 = 0.5. The recombinant proteins were induced with 0.3 mM isopropyl b-D-thiogalactoside (IPTG) for 20 h at 18°C. Bacterial cells were collected and affinity-purified with Ni-NTA agrose (QIAGEN, for pColdTM TF constructed plasmids) and Amylose Resin (New England Biolabs, for pMAL-c5X constructed plasmids), following manufacturer's instructions.

For *in vitro* ubiquitination reactions, 1 μg of MBP-RIP1, MBP-APIP6, MBP-RIP1 H74Y or MBP-APIP6 (H58Y) were incubated with wheat E1 (50 ng), *Arabidopsis* E2 (UBC10, 200 ng), 1 μg of ubiquitin, and 1.5 μL of 20 × reaction buffer (1 M Tris HCl pH 7.5, 40 mM ATP, 100 mM $MgCl_2$, 40 mM DTT, 600 mM creatine phosphate, and 1 mg/mL creatine phosphokinase). After incubation at 30°C for 1.5 h, the reaction was stopped by adding SDS loading buffer and heating at 100°C for 5 min. Samples were then separated on a 10% SDS-PAGE gel. Ubiquitination signals were detected by immunoblotting with anti-ubiquitin, anti-MBP, and anti-ROD1 antibodies, respectively.

Catalase Activity Assay

Rice leaf samples were ground into fine powders in liquid nitrogen. 1 g of each sample was suspended in 2 mL extraction buffer (50 mM Tris-HCl, pH 7.5, 150 mM NaCl, 0.5% Triton X-100, 10% glycerol, and 1% protease inhibitor cocktail) and centrifuged at 12, 000 rpm for 15 min at 4°C. Protein concentration was measured using a BCA protein assay kit (CWBIO). The supernatant was used for catalase activity analysis with the Catalase Assay Kit (Beyotime) according to the manufacturer's instructions. The activity of purified CatB was measured as the absorbance decrease at 240 nm in 50 mM KH_2PO4 and 20 mM H_2O_2 and was shown as units/mg (Weydert and Cullen, 2010). One unit represents the amount of enzyme that catalyzes the decomposition of 1 μM H_2O_2 per minute at 25°C. To assess the effect of ROD1 and AvrPiz-t on CatB activity, various concentrations of purified ROD1 or AvrPiz-t proteins were mixed with CatB for 1 h at 4°C, and catalase activity was then determined.

Microscale Thermophoresis (MST) Assay

MST was used to quantify the Ca^{2+} binding affinities of ROD1, ROD1^{D132N}, ROD1$^{D\text{-}quad}$, and AvrPiz-t as previously reported (Yang et al., 2019). In brief, recombinant proteins ROD1-TF, ROD1^{D132N}-TF, ROD1$^{D\text{-}quad}$-TF and AvrPiz-t-TF (*ROD1*, ROD1^{D132N}, *ROD1*$^{D\text{-}quad}$ and AvrPiz-t were amplified and inserted into the vector pCold^{TM} TF) with His6-tag were purified from *E. coli* DE3 as described above. A volume of 100 μL (10 μM) purified ROD1, ROD1^{D132N}, ROD1$^{D\text{-}quad}$ and AvrPiz-t proteins were exchanged into a labeling buffer and labeled by the dye NT-647-NHS (Nano Temper Technologies GMBH, MuÈnchen) at room temperature for 30 min in the dark. The labeled protein was displaced by MST buffer containing 50 mM Tris-HCl (pH 8.0), 150 mM NaCl and

0.05% (V/V) Tween-20. 16 small micro reaction tubes were labeled from 1 through 16. 20 μL of the highest concentration $CaCl_2$ (60 μM for ROD1, and 100 mM for $ROD1^{D132N}$, $ROD1^{D\text{-}quad}$ and AvrPiz-t) in MST buffer was filled into the first micro reaction tube 1, and 10 μL of MST buffer was filled into the micro reaction tubes 2 to 16. 10 μL of tube 1 was transferred to tube 2 and mix well by pipetting up and down several times. A serial dilution was obtained by repeating 15 times and remove 10 μL from tube number 16 after mixing. A range of concentrations of calcium ion ($CaCl_2$) were diluted serially from 60 μM to 1.831 nM for ROD1 and 100 mM to 3.05 μM for $ROD1^{D132N}$, $ROD1^{D\text{-}quad}$ and AvrPiz-t in MST buffer. 10 μL of labeled proteins were mixed with 10 μL of calcium ion ($CaCl_2$) at double the concentration determined before in MST buffer. The samples in tubes 1 to 16 were incubated at room temperature for 10 minutes, and then loaded into silica capillaries (Polymicro Technologies). Binding reactions were measured using a microscale thermophoresis instrument (Nano Temper Technologies GMBH) at 25°C, 40% MST power and 20% LED power. The KD Fit function of the Nano Temper Analysis Software MO Affinity Analysis (V2.3) was used to fit the curve and calculate the value of the dissociation constant (K_d).

Lipid-Protein Binding Assay

To test the lipid binding affinities of ROD1 and AvrPiz-t, we performed *in vitro* lipid-protein binding assay (Okazaki et al., 2015). The coding sequences of *ROD1*, *ROD1* Ca^{2+} binding mutants, and *AvrPiz-t* were amplified with primers. The fragments were cloned into vector pGEX-4T-3 vector (GE Healthcare), and transformed into *Escherichia coli* BL21 (DE3) cells. Isopropylthio-β-galactoside (0.2 mM) was added to induce the expression of the recombinant proteins. Cells were harvested at 6 hours after induction and suspended in PBS buffer. After sonication, the recombinant ROD1 and AvrPiz-t proteins were purified with GST-tag beads (GE Healthcare).

For lipid-protein binding assay, the lipid strips (P-6001; Echelon Biosciences) were first blocked in PBS-T containing 0.1% v/v Tween-20 and 3% BSA for one hour at room temperature (RT). Purified ROD1-GST, $ROD1^{D\text{-}trip}$-GST, and AvrPiz-t proteins (1.0 μg/mL) were incubated with the lipid strip membranes for two hours at room temperature with gentle agitation. After washing in PBST for five times, the membranes were then incubated with an anti-GST antibody for two hours at room temperature. The hybridization signals were detected using the ECL systems and images were captured using the Tanon-5200 Chemiluminescent imaging system (Tanon).

Cell Death Assay in Nicotiana benthamiana

We used the *N. benthamiana* cell death assay to determine the functions of ROD1 and catalase in suppressing the hypersensitive response induced by MLA10 (Bai et al., 2012). The coding sequences of ROD1, CatB, and MLA10 were amplified using gene specific primers, and cloned into the vectors pCAMBIA1300-35S-eGFP(C)-rbcsE9, pCAMBIA1305-Flag and pCAMBIA1300-35S-HA(C)-rbcsE9, respectively. The resulting constructs were transformed into *Agrobacterium tumefaciens* strain GV3101. After culture in LB medium overnight at 28°C, the concentrations of GV3101 carrying various constructs were adjusted to OD600 = 1.0, and mixed with a GV3101 strain that expresses p19. The Agrobacteria suspensions were kept at RT for three hours without shaking, and then infiltrated into the leaves of three-week-old *N. benthamiana* plants. Infiltrated leaves were collected at 36 hpi after transformation, and the expression of each protein was confirmed by immunoblotting using anti-GFP, anti-FLAG and anti-HA antibody, respectively. ROS accumulation was detected at 36 hpi by DAB staining. Cell death on infiltrated leaves was photographed at 48 hpi, and quantified by measuring the relative gray area.

DAB Staining

Accumulation of H_2O_2 was detected by 3,3′-diaminobenzidine (DAB) staining as described previously (Yin et al., 2018). Leaf tissues were cut into small pieces (~1cm in length) and vacuum-infiltrated in DAB solution [1mg/mL DAB, 10 mM MES, pH 3.8 with 0.2% (v/v) Tween-20] for 5 min. After further incubation at 25°C for 8 h, samples were cleared by boiling in 96% ethanol for 10 min. The cleared samples were mounted in 50% glycerol for imaging.

mRNA *in situ* Hybridization

We used *in situ* hybridization to examine gene expression patterns in rice tissues. cDNA fragments from each gene were amplified and ligated into the pGEM®-T Easy vector (Promega). The insertion orientation of each fragment was verified by sequencing. The constructs were used as templates for PCR with T7 and SP6 primers. The PCR products were purified and used for *in vitro* transcription with the DIG RNA Labeling Kit (Roche). Shoot apices and leaves of rice wild-type TP309 plants were fixed in FAA (3.7% formaldehyde, 5% acetic acid, 50% ethanol), embedded in wax and cut into 8-μm sections. The slices were treated, as described previously (Yang et al., 2017), in Histoclear II (National Diagnostics, HS-202) for 2 times with each treatment 10 min, and were further treated in EtOH for 2 times with 2 min each. The tissue sections were then treated in the following buffers: 95% EtOH, 1 min; 90% EtOH, 1 min; 80% EtOH, 1 min; 60% EtOH/0.75% NaCl, 1 min; 30% EtOH/0.75% NaCl, 1 min; 0.75% NaCl, 2 min; PBS, 2 min; Proteinase K (19.2 mg/ml), 37°C, 30 min; glycine (2mg/ml in PBS), 2 min; FAA, 5 min; PBS, 2 times, 5 min each. For dehydration, the samples were treated in the following buffers: 0.75% NaCl, 2 min; 30% EtOH/0.75% NaCl, 30 s; 60% EtOH/0.75% NaCl, 30 s; 80% EtOH, 30 s; 90% EtOH, 30 s; 95% EtOH, 30 s; 100% EtOH, 1 min; 100% EtOH fresh, 1 min. The sections were then hybridized with gene-specific probes at 55°C overnight, and incubated with an anti-digoxigenin antibody (Roche) for two hours at RT. The hybridization signals were detected by the color reaction using NBT/BCIP (Roche).

qRT-PCR

For quantification of gene expression, total RNAs were extracted from different tissues using the TRIzol reagent according to the manufacturer's instructions (Invitrogen). 2 μg RNA was reverse-transcribed into cDNA using oligo (dT) primer and SuperScript III reverse transcriptase (Invitrogen). The cDNAs were used as templates for PCR with gene-specific primers (Table S3). Quantitative real time RT-PCR analysis (qRT-PCR) was performed using SYBR Premix Ex Taq (TaKaRa) and gene-specific primers (Table S3). All experiments were repeated three times independently.

RNA-seq Analysis

RNA-seq was performed by BGI (Shenzhen, China). Raw data (raw reads) were processed by NGS QC Toolkit_v2.3.340 and mapped to the Nipponbare reference genome. The read counts of each gene were obtained by htseq-count-0.7.243. DESeq functions were used to identify the differentially expressed genes ($p < 0.05$ and fold change ≥ 1.5). Three biological replicates of different plants were used for RNA seq analysis. The whole sequencing data were deposited in a public data source.

SA and JA Measurement

Rice plants grown in the paddy field were used for SA and JA measurement as previously described (You et al., 2016). Total JA and SA were extracted from the second leaves of 45-day-old plants. SA was analyzed using an HP1100 high-performance liquid chromatography (HPLC) system (Agilent Technologies, Santa Clara, CA) with *o*-anisic acid (Sigma-Aldrich, St Louis, MO) as the internal standard. JA was analyzed by gas chromatography-mass spectrometry (GC-MS) with the labeled D3-JA as an internal standard. All experiments were performed with three biological repeats.

Measurement of H_2O_2

Quantification of H_2O_2 was performed using an Amplex Red hydrogen peroxide/peroxidase assay kit (Molecular Probes), following the manufacturer's instructions. The samples were frozen in liquid nitrogen and ground into fine powders. 100 mg of each sample was fully suspended in 1 mL H_2O_2 extraction buffer (20 mM sodium phosphate buffer, pH 6.5). The extracts were centrifuged at 12,000 rpm for 10 min at 4°C, and the supernatant was used for the quantitative assay. The concentration of H_2O_2 was shown as μM/g fresh weight.

Detection of ROS

ROS measurement with luminol-based approach was performed as previously described (Park et al., 2012) with some modifications. Briefly, leaf sheaths from 10-day-old rice plants cultivated on 1/2 MS medium were collected (approximately 3 mm strips) and floated on sterilized water overnight for recovery. The leaf sheaths were then treated with 1 μM flg22 or water in reaction buffer containing 20 μM of luminol (Wako) and 10 μg/mL of horseradish peroxidase (Sigma). Luminescence was monitored immediately after the treatment, and continuously measured at 1-min intervals for 100 minutes with Varioskan Flash multireader (Thermo Fisher Scientific).

Protein Subcellular Localization

The subcellular localization of ROD1, ROD1 mutants, was analyzed in rice protoplasts prepared from leaf sheaths of 10-day-old TP309 seedlings. The coding regions of *ROD1* and the mutated forms were amplified using primers pA7-ROD1-F and pA7-ROD1-R (Table S3). All fragments were inserted into pA7-YFP, and transformed into rice protoplasts. Expression of fusion proteins was examined under confocal microscopy (Zeiss LSM510 and Leica TCS SP8).

Protein Homology Modeling

The structures of AvrPiz-t and the C2B domain of vesicle exocytosis protein Munc13 were retrieved from the reported Protein Data Bank database under the PDB numbers 2LW6 and 6NYT, respectively. 6NYT was used as a template for modeling the topologies of ROD1 and its core C2 domain. Homology modeling was performed using the Swiss model online service program (https://swissmodel.expasy.org/interactive#structure). All PDB data were visualized and processed in the PyMol Molecular Graphics System (version 2.0; Schrödinger).

Phylogenetic Analysis

Protein sequences of ROD1-like C2 domain proteins were retrieved from Phytozome (https://phytozome-next.jgi.doe.gov/pz/portal.html). The amino acid sequence of ROD1 was used as a query to search the proteome database of 64 plant species listed in Phytozome 12.1 using the BLASTP program with an Expect (E) threshold of '-1'. Multiple sequence alignments of protein were done in Clustal X (1.83). A phylogenetic tree of aligned sequence was constructed in MEGA7 using the Maximum Likelihood method.

SNP and Local Adaptation Analysis

The complete list of high-quality SNPs (produced by the 3K Rice Genomes Project (Wang et al., 2018) within the *ROD1* gene (*Os06g0128800*) and its surrounding regions (with 50 Kb flanking sequence on both sides) was retrieved from the Rice SNP-Seek Database (https://snp-seek.irri.org). The retrieved list of SNPs was further compared with the rice reference genome gene table from RPAN (https://cgm.sjtu.edu.cn/3kricedb/gene-table.php) to obtain the gene-specific SNP list for each enclosed genes and converted it

into the VCF format. In the case of overlapping genes, we selected the leftmost one to represent the corresponding locus. For each gene locus, the nucleotide diversity (Pi) and Tajima's D statistics were calculated using VCFtools v.0.1.17 for both the overall rice population (denoted as "all") and each rice subpopulations (defined by the 3K Rice Genomes Project, Wang et al., 2018).

QUANTIFICATION AND STATISTICAL ANALYSIS

Quantification analysis on lesion areas, pathogen growth, CatB activity, H_2O_2 accumulation, grain production and other measurements were conducted in GraphPad Prism 8 (GraphPad Software, San Diego, CA) and PASW Statistics 18 software. All values are presented with mean ± SD. Exact values of n are indicated in the figures or the legends. Significance of difference was examined by Student's t test and Duncan's new multiple range test. Detailed descriptions of quantifications and statistical analyses can be found in the figures, figure legends, or methods section. No methods were used for sample randomization or sample size estimation and no data were excluded from analyses.

ADDITIONAL RESOURCES

This study did not generate any additional resources.

CellPress
OPEN ACCESS

Supplemental figures

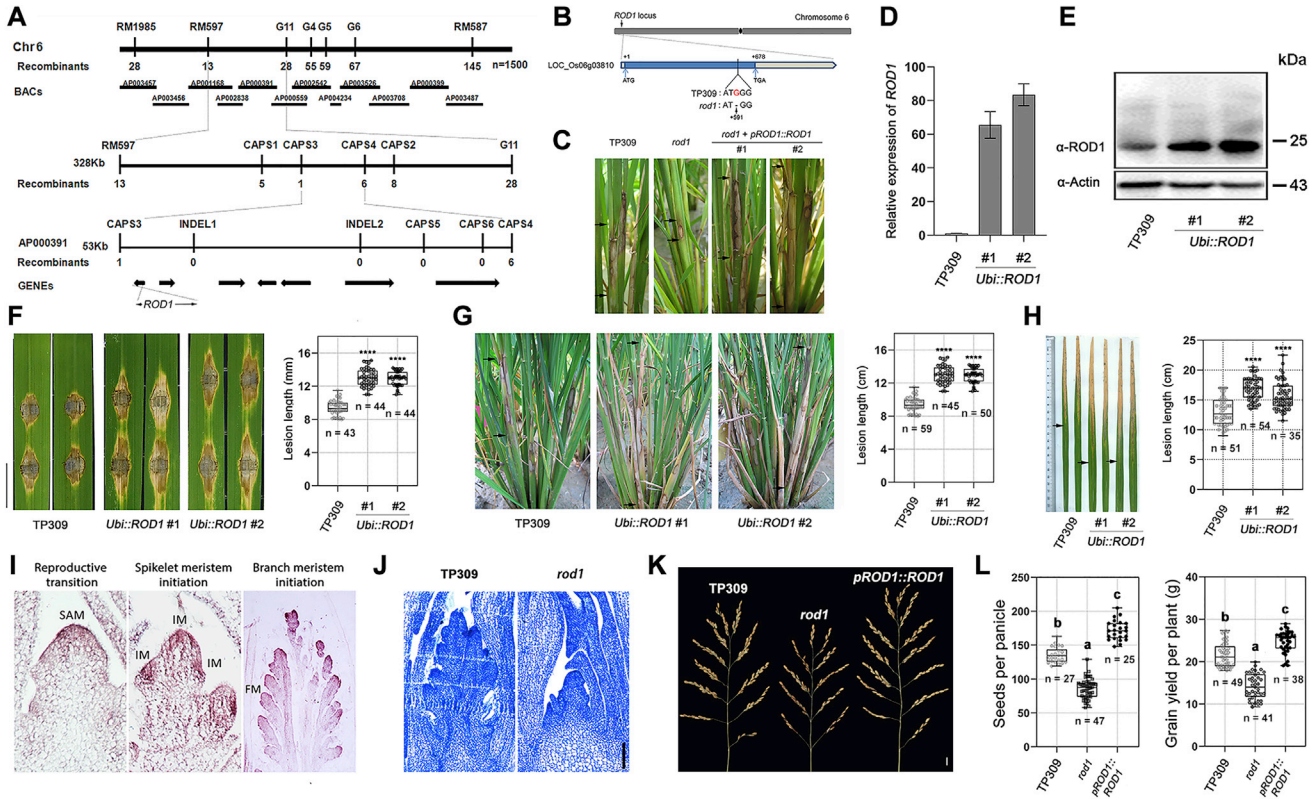

Figure S1. *ROD1* coordinates rice disease resistance and reproductive growth, related to Figure 1

(A) Map-based gene cloning of *ROD1*. *ROD1* was preliminarily mapped to a region near the telomere of chromosome 6, between two simple sequence repeat (SSR) markers RM587 and RM597. With a large mapping population (~10,000 mutant individuals), and newly developed INDEL (Insertion/Deletion) and CAPS (Cleaved Amplified Polymorphic Sequences) markers, *ROD1* locus was narrowed down to a 53-kb DNA region.

(B) Comparison of the 53-kb DNA sequences in wild-type (TP309) and *rod1* revealed a single nucleotide deletion in the exon of *LOC_Os06 g03810*, resulting in a truncation mutant of *ROD1*.

(C) Resistance to sheath blight of lines carrying the candidate *ROD1* gene with its native promoter in *rod1* plants.

(D, E) Detection of *ROD1* mRNA (D) and protein (E) levels in TP309, *rod1*, and overexpression plants. ROD1 proteins were detected by immunoblotting using an anti-ROD1 antibody, and mRNAs were detected by real-time PCR (qPCR). Rice Actin served as a loading control. Error bars in (D) represent mean ± SD (n = 3).

(F-H) Overexpression of *ROD1* decreased rice resistance to blast (F), bacterial blight (G), and sheath blight (H). Scale bar in (F), 5 mm. ****$p < 0.0001$ by two-tailed t test and Bonferroni correction for multiple (two comparisons) tests.

(I) Expression of *ROD1* in rice inflorescence primordia as detected by *in situ* hybridization, showing the enrichment of *ROD1* mRNA in meristematic cells. SAM, shoot apical meristem; IM, inflorescence meristem; FM, floral meristem.

(J) Microscopic morphology of developing inflorescence primordia in w and *rod1*. Note that inflorescence development is delayed in *rod1*. Scale bar, 100 μm.

(K), (L) *ROD1* promotes panicle development (K) and grain production (L). *rod1* mutant plants developed smaller panicles, whereas overexpression of *ROD1* in TP309 (*pROD1::ROD1*) increased panicle size and grain production. Significant differences in (L) were determined by Duncan's new multiple range test and indicated with different letters.

Data in (F, G, H, L) are displayed as box and whisker plots with individual data points. The error bars represent maximum and minimum values. Center line, median; box limits, 25th and 75th percentiles.

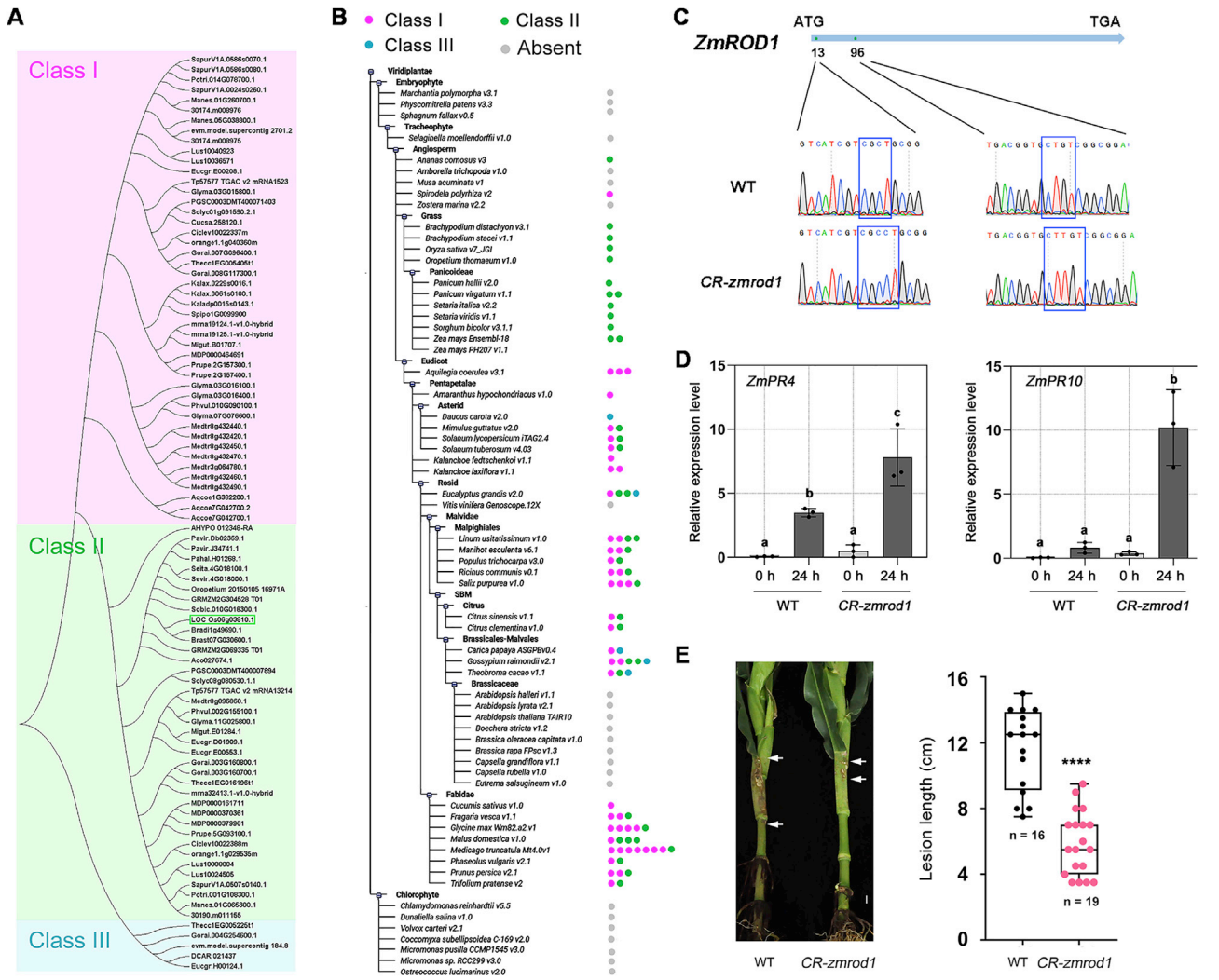

Figure S2. Conserved functions of *ROD1* ortholog in maize immune suppression, related to Figure 1

(A) A phylogenetic tree of C2 domain proteins with sequence homology to ROD1 (BLASTP, E threshold = −1) was constructed in MEGA7 using the Maximum-Likelihood method. ROD1-like proteins are grouped into three clades, with ROD1 (LOC_Os06G03810) being in Class II, labeled with a green outline.

(B) The number of ROD1-like C2 domain proteins in various plant species. The left panel shows a taxonomic tree of plant species in Phytozome with sequenced genomes. Each dot represents one homolog (right). Gray dots mean no ROD1-like proteins. Note that the model plant *Arabidopsis* lacks the *ROD1* ortholog gous gene.

(C) Generation of *ZmROD1* knockout lines by CRISPR/Cas9. The *CR-zmrod1* mutant contains two insertions, C and T, in the target regions, respectively.

(D) Increase of *PR* gene induction in *CR-zmrod1* mutant plants in comparison with wild-type during *R. solani* infection. Significant differences were determined by Duncan's new multiple range test and indicated with different letters. Error bars, mean ± SD (n = 3). Scale bar, 2 cm.

(E) The maize *zmrod1* mutant plants enhanced resistance to *R. solani* in comparison with the wild-type control. The lesion length was measured at 7 dpi. Data are displayed as box and whisker plots with individual data points. The error bars represent maximum and minimum values. Center line, median; box limits, 25th and 75th percentiles. ****p < 0.0001 (two-tailed t test, compared to WT).

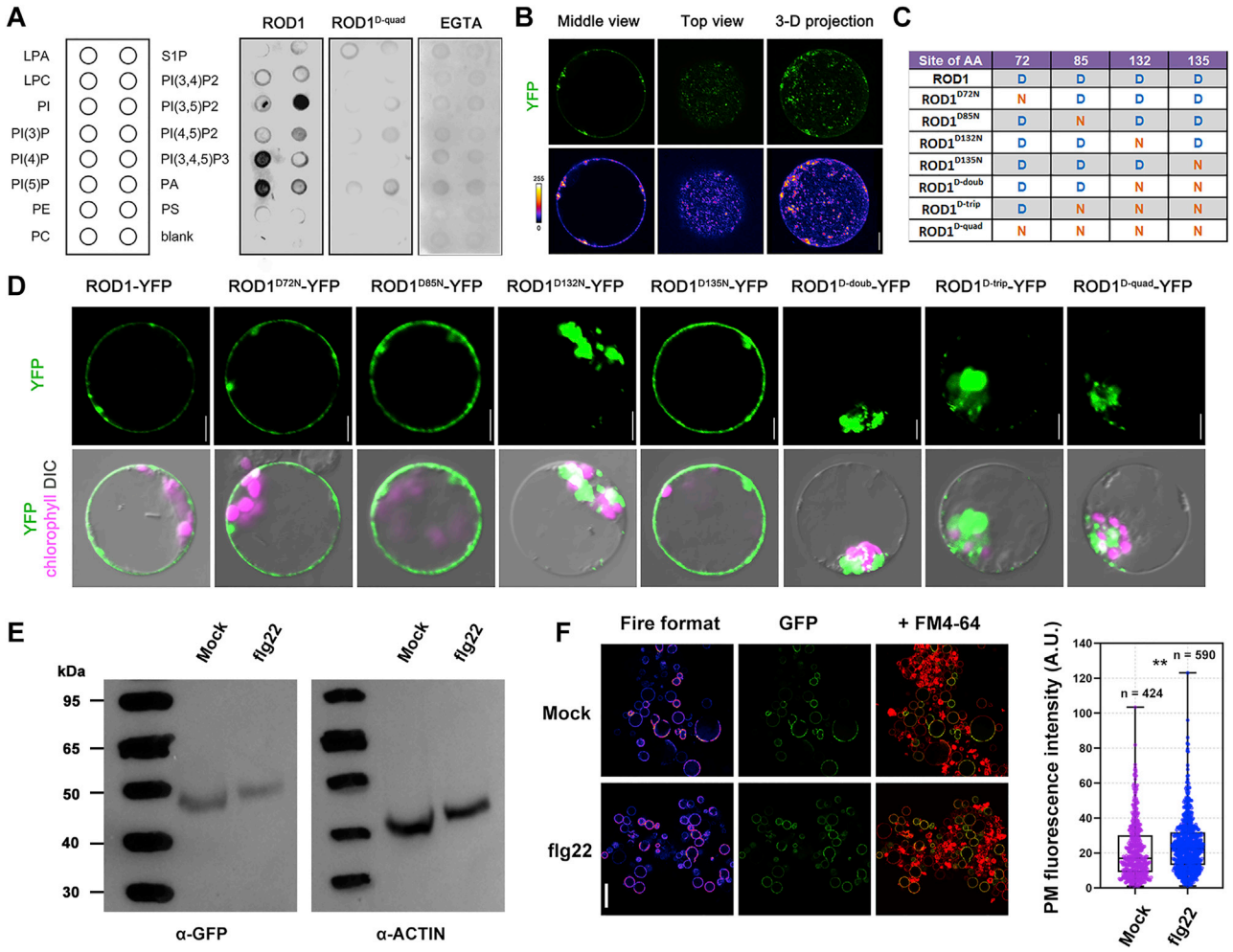

Figure S3. Ca^{2+}-dependent lipid binding and plasma membrane localization of ROD1, related to Figure 2

(A) Phospholipid binding activity of ROD1 and the quadruple mutant $ROD1^{D\text{-}quad}$. In $ROD1^{D\text{-}quad}$ aspartic acids (D) were substituted with asparagine (N). Purified ROD1-GST and $ROD1^{D\text{-}quad}$-GST proteins produced in *E. coli* were incubated with strips containing immobilized phospholipids and detected by immunoblotting using an anti-GST antibody. A schematic diagram of the PIP strip is shown on the left. Note that $ROD1^{D\text{-}quad}$ completely lost phospholipid binding activity. Inclusion of EGTA, a specific Ca^{2+} chelator, also inhibits ROD1 lipid binding.

(B) ROD1-YFP proteins accumulate in small puncta in the plasma membrane (upper panels). Bottom panels are the fire format of YFP fluorescence signals to show the relative fluorescence intensity of ROD1 labeled dots. Scale bars, 5 μm.

(C) Different mutations of ROD1 Ca^{2+} binding sites. D: aspartic acid; N: asparagine.

(D) Subcellular localization of ROD1 Ca^{2+} binding mutants in rice protoplasts. Note that the double, triple, quadruple and D132N variants of ROD1 influenced subcellular localization of fusion proteins. Scale bar, 5 μm.

(E, F) Immune activation promotes ROD1 plasma membrane (PM) localization. ROD1-YFP was expressed in rice protoplasts under the control of the 35S promoter, which were subjected to elicitor (flg22) treatment. The total protein level was likely unchanged after flg22 treatment as revealed by immunoblotting (E), however, the PM proportion of ROD1-YFP proteins was greatly increased as determined by YFP signal intensity in the PM (F). Data in (F) are displayed as box and whisker plots with individual data points. The error bars represent maximum and minimum values. Center line, median; box limits, 25th and 75th percentiles. **$p < 0.01$ (two-tailed t test, compared to mock treatment).

A

Name	Putative function	Y2H frequency
RIP1	**zinc finger C3HC4 domain protein**	**27**
RIP2	Cys-rich domain protein	22
RIP3	MATH domain protein	16
RIP4/APIP6	**zinc finger C3HC4 domain protein**	**10**
RIP5/CatB	**catalase isozyme B**	**9**
RIP6	TPP binding domain protein	8

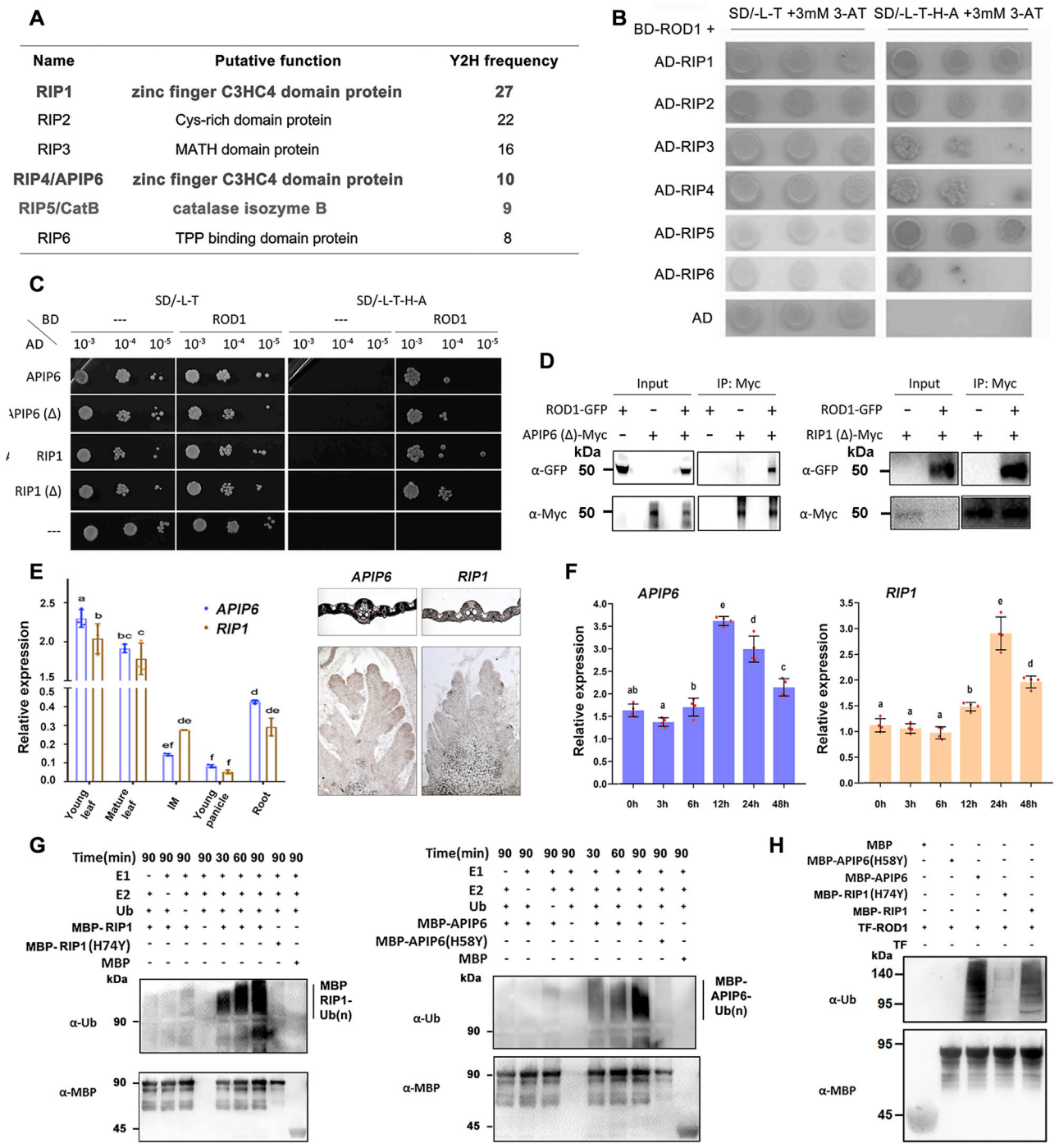

Figure S4. Ubiquitination of ROD1 by the E3 ligases RIP1 and APIP6, related to Figure 3

(A, B) The candidate proteins revealed by the Y2H screen (A) that interact with ROD1 in yeast (B).

(C) ROD1 interacts with both full-length and truncated RIP1 and APIP6 proteins in yeast. RIP1(Δ) and APIP6(Δ) are E3 ligase mutants with the RING domain deleted.

(D) Detection of ROD1 interaction with RIP1 and APIP6 by co-immunoprecipitation (co-IP) in *N. benthamiana* leaves. Due to the instability of full length RIP1 and APIP6 proteins *in planta*, truncated versions lacking the RING domain were used for the interaction assay.

(E) Expression of *RIP1* and *APIP6* in different tissues, as detected by qPCR (left panel) and *in situ* hybridization (right panels). Both *RIP1* and *APIP6* mRNAs were highly expressed in leaves but not in inflorescence meristem (IM). Error bars, mean ± SD (n = 3).

(F) Induction of *RIP1* and *APIP6* expression by pathogen infection. Field-grown plants were inoculated with *Xoo* at the booting stage, and leaf samples were collected during a 0-48 hpi time course. *RIP1* and *APIP6* transcript levels were detected by qRT-PCR. Error bars, mean ± SD (n = 3).

(legend continued on next page)

(G) E3 ubiquitin ligase activity assay of RIP1 and APIP6. Purified MBP-RIP1, MBP-APIP6, MBP-RIP1(H74Y), and MBP-APIP6 (H58Y) proteins were incubated with E1 (*Triticum aestivum* E1, 40 ng), E2 (AtUBC10, 200 ng), and ubiquitin (AtUBQ14, 1 μg). MBP-RIP1(H74Y) and MBP-APIP6 (H58Y) are RING finger domain mutants, which lose the ligase activity and serve as negative controls.

(H) Ubiquitination of ROD1 by RIP1 and APIP6, as detected by the E3 ubiquitin ligase activity assay. An anti-ubiquitin antibody was used for the immunoblotting. The experiment was repeated for two times in (D, G, H) with similar results. Significant differences in (E, F) were determined by Duncan's new multiple range test and indicated with different letters.

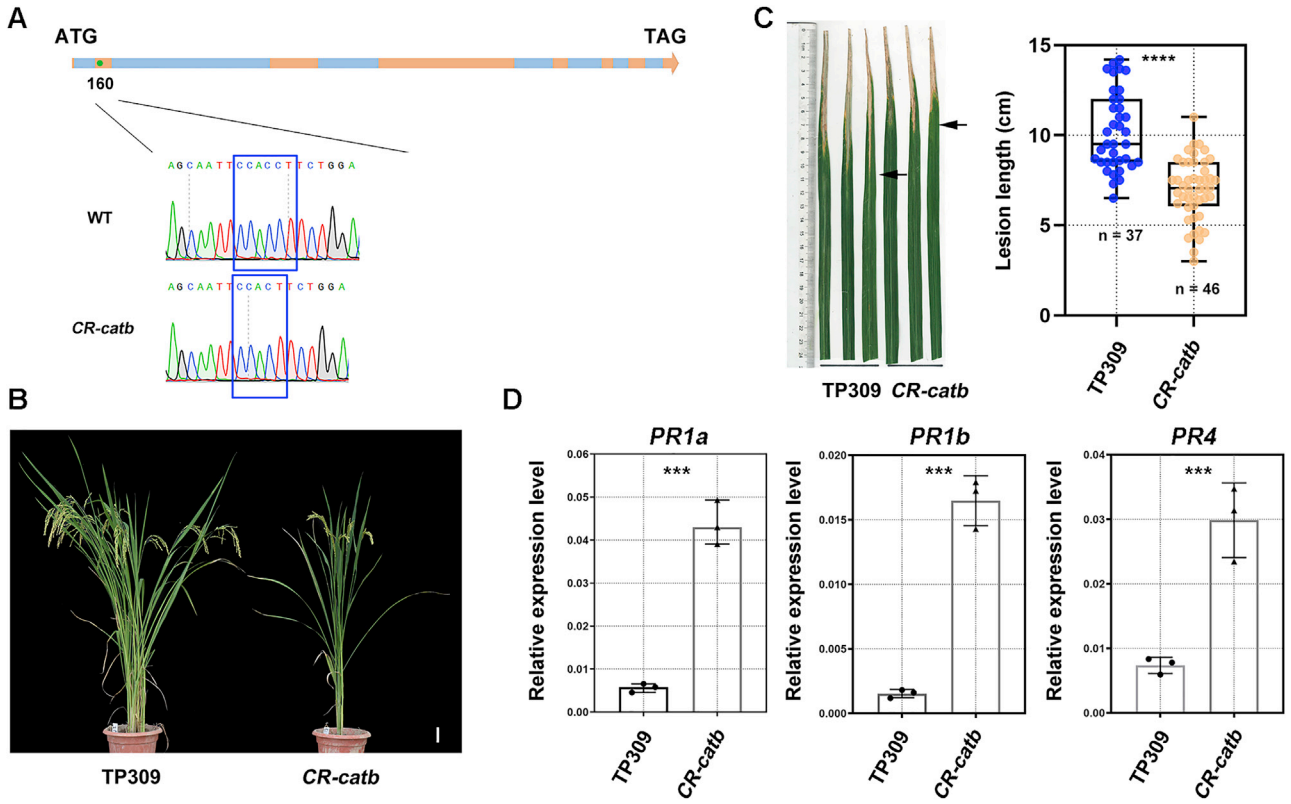

Figure S5. Enhanced disease resistance in *CatB* CRISPR/Cas9 mutant, related to Figure 4

(A) Generation of the *CatB* CRISPR/Cas9 mutant. The *CR-catb* mutant carries a 1 bp deletion in the target region.

(B) Morphology of TP309 and *CR-catb*. The *CR-catb* mutant showed a growth defect. Scale bar, 5 cm.

(C) Increased bacterial blight resistance in *CR-catb*. Leaves were inoculated with Xoo strain PXO99A. The lesion length was measured at 14 dpi. Data are displayed as box and whisker plots with individual data points. The error bars represent maximum and minimum values. Center line, median; box limits, 25th and 75th percentiles. ****$p < 0.0001$ (two-tailed t test, compared to TP309).

(D) Increase of *PR* gene expression in *CR-catb*. Error bars, mean ± SD (n = 3). ***$p < 0.001$ (two-tailed t test, compared to TP309).

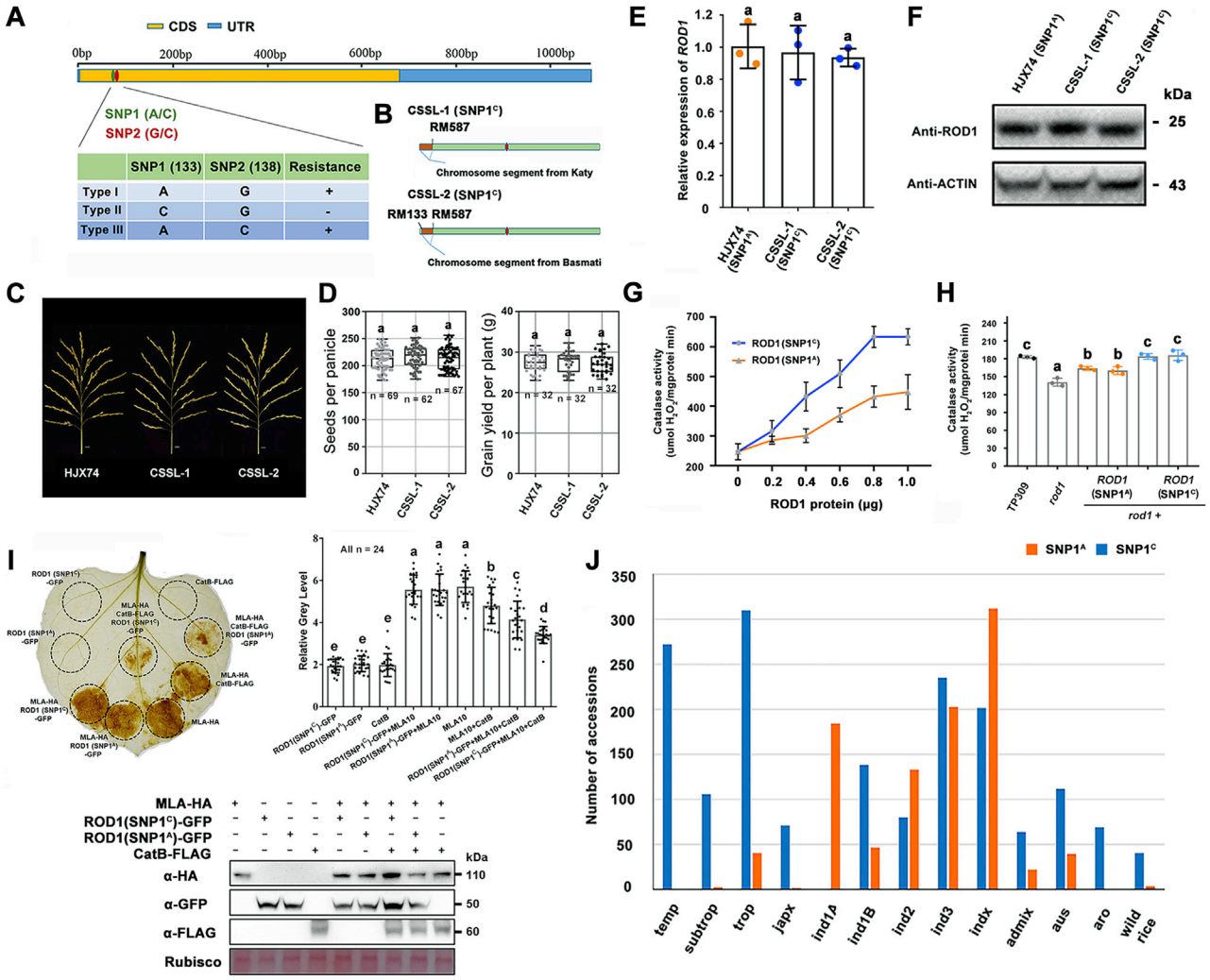

Figure S6. Comparison of SNP1^{A} and SNP1^{C} functions in immune suppression, related to Figure 5

(A) Three types of *ROD1* haplotypes with SNP1 and SNP2 identified in cultivated rice varieties. Note that SNP1$^{A/C}$ results in amino acid substitution.

(B) Development of chromosome segment substitution lines, CSSL-1 (Katy) and CSSL-2 (Basmati) with SNP1^{C} in HIX74 (SNP1^{A}).

(C), (D) Panicle development (C) and grain production (D) showed no difference in HJX74 with SNP1^{A} and the two CSSL lines with SNP1^{C}. Significant differences in (D) were determined by Duncan's new multiple range test and indicated with different letters.

(E) *ROD1* transcript levels were not changed in the two CSSL lines in comparison with the parent variety HJX74. Significant differences were determined by Duncan's new multiple range test and indicated with different letters (n = 3).

(F) ROD1 protein levels were comparable between HJX74 and the two CSSL lines. An anti-ROD1 antibody was used to detect ROD1(SNP1^{A}) in HJX74 and ROD1(SNP1^{C}) in the two CSSL lines. The rice Actin protein was detected as a loading control.

(G) Comparison of ROD1(SNP1^{A}) and ROD1(SNP1^{C}) activities in activation of CatB-mediated H_2O_2 degradation. Purified CatB protein was used for the *in vitro* catalase assay in the presence of different amounts of ROD1 proteins. Note that ROD1(SNP1^{C}) displayed higher CatB-promoting activity than ROD1(SNP1^{A}) (n = 3).

(H) Comparison of catalase activity of total proteins extracted from TP309, *rod1*, and *rod1* complemented with *ROD1*(SNP1^{A}) and *ROD1*(SNP1^{C}). *ROD1*(SNP1^{A}) could not fully restore catalase activity in the two representative *ROD1*(SNP1^{A})/*rod1* complementation lines, in contrast to *ROD1*(SNP1^{C})/*rod1* that fully restored wild-type catalase activity. Significant differences were determined by Duncan's new multiple range test and indicated with different letters (n = 3).

(I) Cell death analysis in tobacco leaves transiently expressing the ROD1 variants, with CatB and ROD1 alone as negative controls, and MLA alone as a positive control. The severity of cell death was quantified and presented as relative gray area, showing that the activity of ROD1(SNP1^{C}) to attenuate MLA10-triggered cell death was stronger than ROD1(SNP1^{A}). Protein expression levels were detected by immunoblot. Ponceau staining of Rubisco is used as a loading control. Different letters at the histogram top indicate a statistically significant difference at $p < 0.05$, by Welch's ANOVA and Bonferroni correction.

(J) Distribution of SNP1^{A} and SNP1^{C} in the twelve rice subpopulations of ~3,000 accessions.

Error bars in (E, G, H, I) represent mean ± SD, in (D) represent maximum and minimum values. Center line, median; box limits, 25th and 75th percentiles. Experiments were repeated two times in (G, H) with similar results.

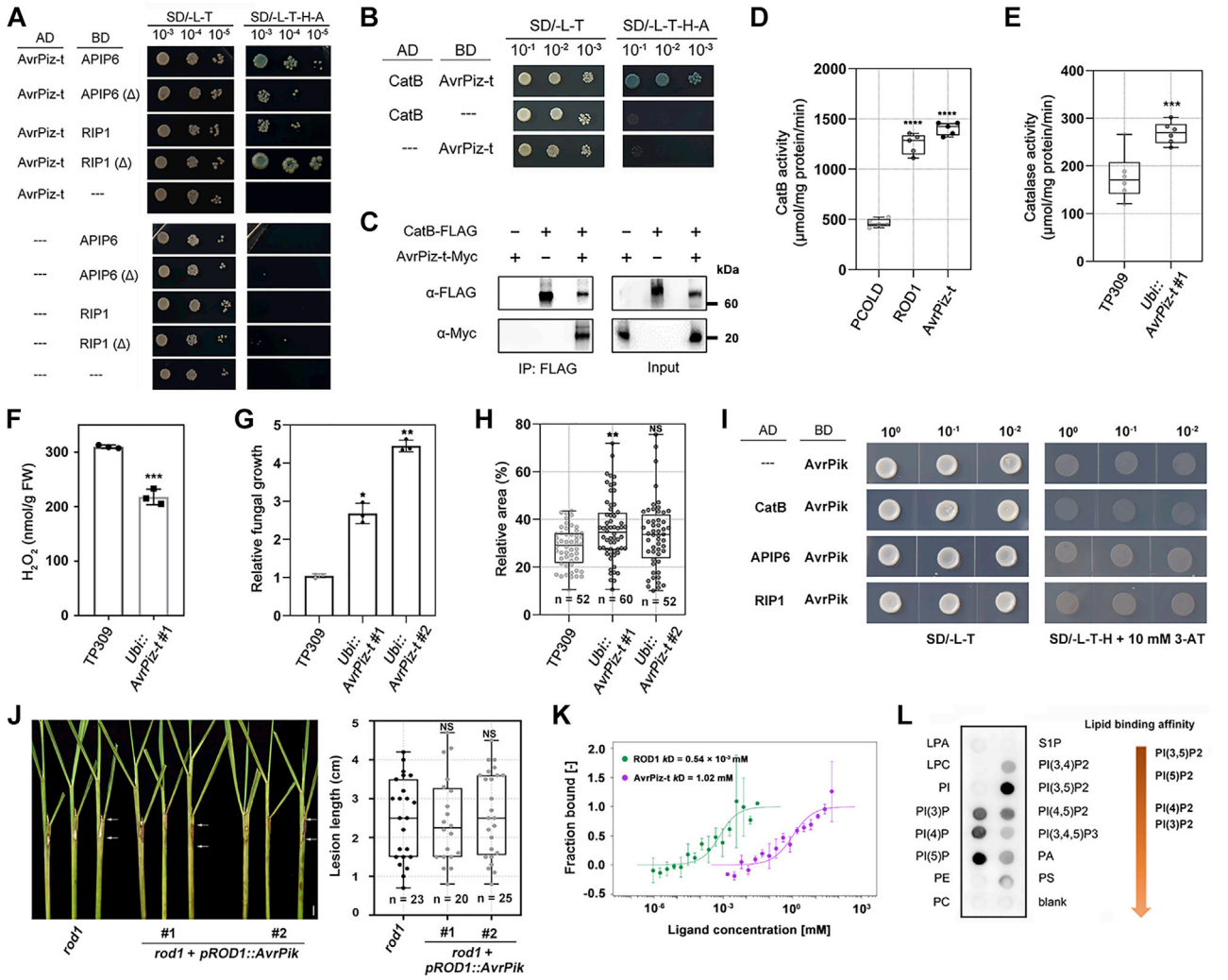

Figure S7. AvrPiz-t promotes CatB activity to suppress H_2O_2 accumulation and disease resistance, related to Figure 6

(A) Interaction of AvrPiz-t with RIP1 and APIP6 with in yeast. AvrPiz-t interacts with both full-length RIP1 and APIP6 as well as their truncated forms lacking the RING domain.

(B, C) Interaction between AvrPiz-t and CatB, as revealed by Y2H (B) and Co-IP (C).

(D) AvrPiz-t facilitates CatB-mediated H_2O_2 degradation. Purified CatB protein was used for the catalase assay in the presence of AvrPiz-t or ROD1 proteins. ****$p < 0.0001$ by two-tailed t test and Bonferroni correction for multiple (two comparisons) tests ($n = 5$).

(E) Overexpression of *AvrPiz-t* in TP309 under the control of the maize ubiquitin promoter enhanced catalase activity. ***$p < 0.001$ (two-tailed t test, compared to TP309) ($n = 6$).

(F) Decreased H_2O_2 levels in *AvrPiz-t* overexpression plants. ***$p < 0.001$ (two-tailed t test, compared to TP309) ($n = 3$).

(G, H) *AvrPiz-t* overexpression plants increased susceptibility to blast (G) ($n = 3$) and sheath blight (H). *$p < 0.1$, **$p < 0.01$, two-tailed t test and Bonferroni correction for multiple (two comparisons) tests. NS, not significant.

(I) AvrPik does not interact with CatB, APIP6, or RIP1 in yeast.

(J) Expression of *AvrPik* under the control of the *ROD1* promoter did not change the disease resistance phenotype of *rod1*. Scale bar, 2 cm. NS, not significant.

(K) MST assay to compare the Ca^{2+} binding activities of ROD1 and AvrPiz-t. AvrPiz-t does not exhibit obvious Ca^{2+} binding capacity. The solid curve is the fit of the data points to the standard KD-Fit function. Each binding assay was repeated independently three times, and bars represent standard deviations. K_d = dissociation constant.

(L) Phospholipid binding activity of AvrPiz-t. AvrPiz-t associates with the similar lipids to ROD1 in this assay.

Error bars in (F, G) represent mean ± SD, in (D, E, H, J) represent maximum and minimum values. Center line, median; box limits, 25th and 75th percentiles. The experiment was repeated for two times in (D, E, F) with similar results.